Convection-generated gravity waves in the tropical lower stratosphere from Aeolus wind profiling, GNSS-RO and ERA5 reanalysis

Mathieu Ratynski^{1,a,*}, Sergey Khaykin¹, Alain Hauchecorne¹, M. Joan Alexander², Alexis Mariaccia³, Philippe Keckhut¹ and Antoine Mangin⁴

Correspondence to: Mathieu Ratynski (mathieu.ratynski@estaca.eu)

Abstract. The European Space Agency's Aeolus satellite, equipped with the Atmospheric LAser Doppler INstrument (ALADIN), provides global provides near-global wind profiles from the surface to about 30 km altitude. These wind measurements enable the investigation of atmospheric dynamics, including gravity waves (GWs) in the upper troposphere and lower stratosphere (UTLS). This study analyzes ALADIN wind observations and ERA5 reanalysis, by deriving GWs kinetic energy (Ek) distributions, examining their temporal and spatial variability throughout the tropical UTLS. A prominent hotspot of enhanced GW activity is identified by Aeolus, migrating from the Indian Ocean in Boreal Summer to the Maritime Continent in Boreal Winter, closely matching outgoing longwave radiation minima and thus highlighting convective origins. Results show that ERA5 consistently underestimates Ek in convective regions, especially over the Indian Ocean, where conventional wind measurements are sparse. Additional comparisons with Global Navigation Satellite System Radio Occultation (GNSS-RO) measurements of GW potential energy (Ep) corroborate these findings and suggest significant underrepresentation of convection-driven wave activity in reanalyses. A multi-instrumental exploratory analysis also allows to verify the empirical grounding of the established Ek to Ep ratio, as well as the wavelength of the waves retrieved by Aeolus. By providing direct wind measurements in otherwise data-sparse regions, Aeolus offers a valuable dataset for evaluating and potentially improving the representation of GWs in reanalyses, particularly in remote tropical areas. The combination of Aeolus and GNSS-RO data allows for an observationally-based examination of the partitioning between kinetic and potential energy, highlighting discrepancies with reanalysis products that could inform future model parameterization development. By filling critical wind data gaps, Aeolus emerges as a key tool for improving the representation of GWs, particularly in remote tropical regions. When combined with GNSS-RO measurements, Acolus data provides new insights into how convective processes drive GW generation, revealing opportunities to refine reanalysis products and model parameterizations, as well as improving the energy ratio.

¹Laboratoire Atmosphère Milieux et Observation Spatiales (LATMOS), Guyancourt, France

²NorthWest Research Associate, Boulder, CO, US

³Program in Atmospheric and Oceanic Sciences, Princeton University, Princeton, New Jersey, United States

⁴ACRI-ST, 260 Route du Pin Montard, Sophia-Antipolis, Biot 06410, France

anow at: Rosenstiel School of Marine and Atmospheric Science, University of Miami, Coral Gables, Florida, United States

1. Introduction

6

19

- 2 Atmospheric reanalysis reanalyses like ERA5, a global atmospheric dataset produced by the European Centre for Medium-
- 3 range Weather Forecasts (ECMWF), are essential for climate assessments and atmospheric research_(Hersbach et al., 2020).
- 4 By integrating observational data with state-of-the-art general circulation models and data assimilation methods, reanalyses
- 5 provide comprehensive atmospheric snapshots for a variety of meteorological research (Muñoz-Sabater et al., 2021).
- 7 However, one significant limitation of these datasets, including ERA5, is their reliance predominantly on temperature
- 8 measurements for data assimilation, with wind measurements being notably sparse (Campos et al., 2022; Podglaien et al.,
- 9 2014). Because of this, ERA5 tends to underestimate low-level wind speeds in certain regions, compared to radiosonde
- 10 measurements (Munday et al., 2022). Having said that, only a relatively few radiosonde and cloud-tracked wind measurements
- 11 directly constrain wind variability: Radiosonde measurements are notably sparse over oceans, as they are typically launched
- 12 from land-based stations, leaving vast oceanic regions under-sampled (Baker et al., 2014; Ladstädter et al., 2011). While some
- 12 Hom land-based stations, leaving vast occurre regions under-sampled (Baket et al., 2014, Ladstadter et al., 2011). White some
- 13 ship-based radiosonde launches occur, they are infrequent and cover limited areas. Satellite cloud-tracking methods, such as
- 14 Atmospheric Motion Vectors (AMVs), provide wind data by tracking cloud movements (Bedka et al., 2009). However, these
- 15 methods have limitations: they cannot retrieve wind profiles in clear-sky conditions and often lack detailed vertical resolution.
- 16 This results in significant observational gaps in wind measurements over oceans and clear-sky regions. This limitation is
- 17 particularly critical when considering atmospheric waves, such as gravity waves, which manifest themselves in temperature
- 18 and wind vertical profiles.
- 20 Gravity waves (GW) play a crucial role in the dynamics of the Earth's atmosphere. Generated by mechanisms such as flow
- 21 over orography, convection, and flow deformation, these waves are instrumental in transporting momentum and energy,
- 22 influencing atmospheric regions far from their origin points (Fritts and Alexander, 2003). While Rossby waves are well
- 23 represented due to their quasi-geostrophic nature, divergent wave modes like gravity waves, Kelvin waves, Rossby-gravity
- 24 waves, and inertia-gravity waves are not sufficiently characterized and must often be parametrized internally by the models
- 25 (Plougonven and Zhang, 2014). The underrepresentation of gravity waves with long horizontal and short vertical scales in
- 26 ERA5 has been highlighted previously (Bramberger et al., 2022).
- 28 For the study period, ERA5 utilizes the non-orographic gravity wave drag (GWD) scheme described by Orr et al., (2010),
- 29 which is based on a spectral approach (Scinocca, 2003; Referred to as S03 in Orr et al., 2010). This scheme does not explicitly
- 30 resolve convectively generated waves based on model-diagnosed convection; instead, it launches a globally uniform and
- 31 constant spectrum of waves from the troposphere. The momentum deposition occurs as these waves propagate vertically and
- 32 interact with the resolved flow via critical-level filtering and nonlinear dissipation. While this parameterization improves the

33 middle atmosphere climate compared to simpler schemes, evaluations have shown it has limitations in fully capturing the 34 required wave forcing, particularly for the Quasi-Biennial Oscillation (QBO) in the tropics (Pahlavan et al., 2021). 35 36 37 Furthermore, even with improvements in reanalysis products, challenges in accurately representing tropical winds persist. 38 Studies of previous-generation reanalyses identified significant errors in tropical regions (Podglajen et al., 2014), and recent 39 work shows that even ERA5's accuracy is highly site-dependent, with notable errors in locations influenced by warm currents 40 (Campos et al., 2022). Furthermore, several studies have identified that the biggest errors in ERA5 reanalysis winds are 41 concentrated in tropical regions and locations influenced by warm currents, showing that the accuracy of these reanalysis is highly site dependent (Podglajen et al., 2014; Campos et al., 2022). This is compounded by difficulties in data assimilation 42 43 systems, such as 4-D var and perfect model scenarios, which struggle to extract circulation information from high-resolution 44 temperature data (Žagar et al., 2004). Despite advancements in the quality of tropical forecasts and analyses, the evidence 45 suggests that radio occultation (RO) data could potentially enable effective long-term monitoring of wind fields globally (Danzer et al., 2023). However, the overall lack of direct wind observations continues to pose significant challenges (Baker et 46 47 48 49 Historically, most GW studies have relied on ground-based or single-use instruments like radiosondes (Zhang and Yi, 2005), 50 rockets (Wüst and Bittner, 2008), or global coverage measurements from the Global Navigation Satellite System Radio Occultation (GNSS-RO). While GNSS-RO provides high-resolution temperature profiling, effectively characterizing GW 51 52 potential energy (Ep) (Fröhlich et al., 2007; Khaykin et al., 2015; Schmidt et al., 2016), it does not capture kinetic energy (Ek), which requires precise wind profiling. 53 54 55 In an effort to bridge many gaps within the observational world, the 2018 launch of the European Space Agency's Aeolus 56 satellite changed our ability to capture atmospheric dynamics, particularly in the upper troposphere and lower stratosphere 57 (UTLS). The UTLS is a region marked by a dramatic increase in static stability at the tropopause, where gravity waves are 58 refracted to shorter vertical wavelengths (Dhaka et al., 2006; Geldenhuys et al., 2023). These waves with short vertical 59 wavelengths (typically 2-10 km) are primarily lower-frequency gravity waves, as dictated by the dispersion relation, and exhibit relatively large amplitude wind variability. The Aeolus satellite, equipped with its Atmospheric LAser Doppler 60 61 INstrument (ALADIN), is able to measure global wind profiles up to an altitude of 30 km, providing insights into the behavior 62 of gravity waves with vertical wavelengths down to ~1.5-2 km in these critical atmospheric layers (Banyard et al., 2021

Code de champ modifié

Mis en forme : Français (France)

Mis en forme : Français (France)

These short wavelength waves are primarily lower frequency gravity waves, as dictated by the dispersion relation, and exhibit

relatively large amplitude wind variability. This is exactly where Aeolus comes into play: Equipped with its Atmospheric

63

64

65

66

Rennie et al., 2021; Ratynski et al., 2023),

insights into the behavior of gravity waves in these critical atmospheric layers (Banyard et al., 2021; Rennie et al., 2021;

Ratynski et al., 2023),

68

67

69

83

70 In this context, this study aims at utilizing Aeolus's global wind profiling capabilities to derive a tropics-wide distribution and variability of the kinetic energy of gravity waves, addressing a gap not typically captured in ERA5 reanalysis. By comparing 71 72 direct measurements with ERA5 data, we reveal certain limitations in the reanalysis's ability to represent tropical gravity wave 73 dynamics. We will look at the most recent reprocessed Aeolus baseline 2B16, providing data from June 2019 to August 2022. Additionally, our study aims at exploring a broader set of analyses, aiming to contextualize the Aeolus wind observations 74 75 within a multi-instrument framework. By comparing Aeolus-derived kinetic energy of GWs with the potential energy estimates 76 from GNSS-RO, we assess the consistency of independent data sources and examine the ratio of kinetic to potential energy in 77 real-world atmospheric conditions. Beyond energy comparisons, we also investigate the vertical wavelength characteristics of 78 convectively generated waves and discuss limitations that arise from Aeolus' bin settings and instrument related noise. With 79 this study, we provide the first observationally-based, tropics-wide estimate of gravity wave kinetic energy from June 2019 to 80 August 2022, directly linking its variability to deep convective sources. With this study, we provide the first observational 81 based three year tropics wide climatology of gravity wave kinetic energy and its link with deep convection, identifying source 82 regions for these waves as emanating from tropical deep convection.

84 The paper will be organized as follows: In Sect. 2, we will discuss the data as well as the methods. It includes a description of the Aeolus, ERA5 and the GNSS-RO datasets, but also explains the horizontal detrending method with its potential and 85 86 limitations. In Sect. 3, we will analyze the wave activity in terms of kinetic energy using Aeolus Rayleigh wind profiling and 87 directly comparing it with ERA5. Additionally, in Sect.4, we broaden our analyses to contextualize Aeolus observations against 88 GNSS-RO data and, criticize the ratio between both elements and determine the wavelength retrieval capability. Finally, the 89 results are discussed in Sect. 5, followed by the conclusions in Sect. 6

2. Data and Methods 90

91 2.1 Instruments and Datasets

92 The Aeolus satellite, with its ALADIN Doppler wind lidar, orbited Earth at a 97-degree inclination and 320 km altitude. Its 93 data consists of 24 vertical range bins that divide the atmosphere (Rennie and Isaksen., 2020), allowing wind profiling between 94 0 and 30 km. Laser pulses and two receivers—Rayleigh and Mie channels—detect the atmosphere's Doppler shifts through 95 molecular and particle backscatter, respectively. The data, organized into atmospheric scenes, cloudy or clear (Rennie and 96 Isaksen, 2020), has an 87 km along-track integration and a vertical resolution varying between 0.25 to 2 km. The distribution 97 of these range bins is determined by a dedicated range bin setting (RBS), which can be adjusted to cater to specific needs, such as enhanced sampling at certain heights. This study uses the Level 2B Rayleigh clear product, with the latest Baseline 2B16 at

Code de champ modifié

Mis en forme: Français (Françe)

Mis en forme : Français (France)

the time of submission, offering the horizontal line of sight (HLOS) wind components. The HLOS wind speed is derived using 100 Aeolus NWP Impact Experiments guidance (Rennie and Isaksen., 2020), with the vertical wind speed assumed to be negligible. 101 A complete description of the instrument, its measurement principles, range bin settings, and data products can be found in 102 Rennie and Isaksen. (2024). The angle θ denotes the azimuth of the target-to-satellite pointing vector, being around 100.5° 103 over the tropics. When injecting the azimuth value into Eq. 1, it becomes apparent that the HLOS wind over the tropics is 104 quasi-zonal.

$$106 \quad v_{HLOS} = -u \sin(\theta) - v \cos(\theta) \tag{1}$$

105

107

108 The ERA5 reanalysis dataset, a European Centre for Medium-Range Weather Forecasts (ECMWF) product, offers 109 comprehensive atmospheric, land-surface, and ocean-wave parameters at hourly resolution and global coverage (Hersbach et 110 al., 2020). Its exceptional horizontal resolution of approximately 33 km at the equator (corresponding to 0.3° 111 latitude/longitude), the best among widely used reanalysis products, enables it to resolve gravity waves with horizontal 112 wavelengths as small as ~100 km (Wright and Hindley, 2018, their table 1). The data products used in this study were retrieved 113 from the ECMWF archive on a regular 0.25° x 0.25° latitude-longitude grid. Additionally, its higher vertical resolution in the 114 troposphere, with 137 vertical levels reaching up to 0.01 hPa, makes it particularly adept at capturing gravity waves with 115 vertical wavelengths down to ~1-2 km. ERA5 also incorporates advanced modelling features such as sponge layers and 116 hyperdiffusion to attenuate artificial wave reflections and stabilize the model numerically, allowing for efficient modelling of large-scale phenomena, notably simulating gravity waves with wavelengths greater than 400 km (Stephan and Mariaccia, 117 118 2021). It is therefore the best a very strong candidate to use as a benchmark for Aeolus' performances. For this study, wind 119 components are retrieved on the native 137 model levels and then interpolated to our high-resolution analysis grid using 120 geopotential height, temperature, and humidity. For this study, wind components are retrieved on standard model levels and 121 converted to specific altitude levels using geopotential height, temperature and humidity.

122 The GNSS-RO method offers many advantages for studying atmospheric dynamics, particularly GW activity and parameters.

123 The first RO-derived GW estimates date back from the early 2000s and several missions have since provided data for further

124 studies, focusing on potential energy as a proxy for retrieving GW activity (Tsuda et al., 2000; Fröhlich et al., 2007; Wang and

Alexander, 2010; Luna et al., 2013; Schmidt et al., 2016), he Radio Occultation Meteorology Satellite Application Facility

125

126 (ROMSAF) provides global GNSS-RO datasets. For the study period of June 2019 to August 2022 these datasets are dominated

127 by the Metop constellation: Metop-B and Metop-C throughout, with Metop-A contributing until its retirement in November

128 2021 (von Engeln et al., 2011). These datasets are derived from the bending angles of GNSS signals as they pass through the

129 Earth's atmosphere and are observed by low Earth-orbiting satellites. It provides global coverage with a high vertical resolution,

130 sub-Kelvin accuracy, full diurnal coverage, and all-weather capability. The vertical resolution of GNSS-RO temperature Code de champ modifié

Mis en forme: Anglais (Royaume-Uni)

Mis en forme: Anglais (Royaume-Uni)

131 profiles is fundamentally limited by diffraction and varies with altitude, typically ranging from ~0.5 km in the lower 132 troposphere to ~1.4 km in the middle atmosphere (Kursinski et al., 1997). While sharp vertical gradients in refractivity (e.g., 133 due to temperature inversions or strong humidity gradients) can be detected, the effective resolution for resolving distinct 134 atmospheric layers is constrained by these diffraction limits. The along-track horizontal resolution is typically around 200-300 135 km. Marquart and Healy (2005) showed that small-scale fluctuations in dry temperature RO profiles could be attributed to 136 GWs with vertical wavelengths equal to or greater than 2 kilometers, Alexander et al. (2008b) suggested analyzing data below 137 30 kilometers in altitude to maintain the signal-to-noise ratio for temperature fluctuations above the detection threshold, which 138 also happens to be Aeolus' maximal capability. Most GW parameters can be derived from single RO temperature profiles. 139 However, estimating momentum flux requires knowledge of the horizontal wave number or wavelength, which cannot be 140 deduced from a single temperature profile. To determine the horizontal structure of GWs, it is necessary to analyze clusters of 141 three or more profiles adjacent in space and time. 142 The GNSS-RO method offers many advantages for studying atmospheric dynamics, particularly GW activity and parameters (Tsuda et al., 2000; Fröhlich et al., 2007; Wang and Alexander, 2010; Luna et al., 2013; Schmidt et al., 2016). The 143 144 Radio Occultation Meteorology Satellite Application Facility (ROMSAF) provides global GNSS-RO datasets, which offer 145 valuable information on atmospheric refractivity, temperature, and geopotential height with high vertical resolution. These 146 datasets are derived from the bending angles of GNSS signals as they pass through the Earth's atmosphere and are observed 147 by low Earth orbiting satellites. It provides global coverage with a high vertical resolution, sub-Kelvin accuracy, full diurnal 148 coverage, and all-weather capability. RO's vertical resolution ranges from 100 meters in the lower troposphere to 1.4 kilometers 149 in the upper stratosphere, with a horizontal resolution of around 300 kilometers. MARQUARDT and Healy (2005) showed that small-scale fluctuations in dry temperature RO profiles could be attributed to GWs with vertical wavelengths equal to or 150 151 greater than 2 kilometers. Alexander et al. (2008b) suggested analyzing data below 30 kilometers in altitude to maintain the 152 signal to noise ratio for temperature fluctuations above the detection threshold, which also happens to be Aeolus' maximal 153 capability. Most GW parameters can be derived from single RO temperature profiles. However, estimating momentum flux 154 requires knowledge of the horizontal wave number or wavelength, which cannot be deduced from a single temperature profile. 155 To determine the horizontal structure of GWs, it is necessary to analyze clusters of three or more profiles adjacent in space 156 and time. The first applications of RO measurements for studying GW activity date back to the early 2000s, and several missions have since provided data for further global GW activity studies (Tsuda et al., 2000; Fröhlich et al., 2007; Wang 157 158 and Alexander, 2010; Luna et al., 2013; Schmidt et al., 2016). These studies have focused on potential energy as a proxy 159 for estimating GW activity. 160 161

Mis en forme: Anglais (Royaume-Uni)

Code de champ modifié

Mis en forme: Anglais (Royaume-Uni)

Code de champ modifié

Mis en forme: Anglais (Royaume-Uni)

Mis en forme: Anglais (Royaume-Uni)

162

163

Although Aeolus' full operational lifespan spans from August 2018 to April 2023, at the time of this study, the entire dataset has not yet been reprocessed, requiring significant effort from the responsible team. Meanwhile, we focus on the most recent reprocessed Aeolus baseline, 2B16, which covers the period from June 2019 to August 2022. This baseline represents the most

up to date dataset available and demonstrates the highest fidelity among all previous baselines. Since ERA5 and GNSS-RO
 have been operational for much longer and remain in use today, we limit the scope of our study to align with the 2B16 baseline
 period.

167

168

temperature profiles, all brought to a standard interpolated grid to facilitate the accurate comparison and integration of data from the different sources. The chosen grid has a vertical resolution of <u>1</u>500 meters and spans a range from 0 to 30 km altitude.

This choice of resolution is close to the dataset's (280 m for ERA5, ~300m for GNSS-RO and 1 km for Aeolus) native

This study specifically utilizes Aeolus Level 2B Rayleigh clear HLOS winds, ERA5 wind components, and GNSS-RO

172 resolution in the UTLS and serves as an acceptable middle ground. This approach preserves the maximum vertical detail from

173 <u>each dataset before analysis.</u>

174

- 175 The choice to compare Aeolus measurements with the ERA5 reanalysis, which does not assimilate Aeolus winds, is intentional.
- 176 This approach allows for a direct assessment of Aeolus's potential contribution by treating it as an independent dataset, thereby
- 177 highlighting regions where its direct wind measurements might fill observational gaps present in the conventional observing
- 178 system assimilated by ERA5.
- 179 The choice to compare Aeolus measurements directly with ERA5, instead of operational Integrated Forecasting System (IFS)
- 180 analyses that assimilate Aeolus winds, is intentional. This comparison method distinctively highlights ERA5's limitations in
- 181 capturing elements of the gravity wave spectrum. By contrasting Aeolus data with ERA5, the study demonstrates Aeolus's
- 182 unique contributions and potential to enhance future reanalyses and forecasting models. While operational IFS analyses
- 183 assimilating Aeolus winds would showcase improved analytical quality, such an approach would obscure the specific
- 184 enhancements brought by the satellite, blending them with the inherent model capabilities

185

186 2.2 Methods and Limitations

- 187 The following section discusses the retrieval of GW kinetic energy, Ek. A primary challenge in this retrieval, particularly in
- 188 the tropical UTLS, is the robust separation of GWs from other dominant, synoptic-to-planetary scale equatorial waves, such
- 189 as Kelvin waves. Observational studies using GNSS-RO data have consistently shown that Kelvin waves, with typical vertical
- 190 wavelengths in the range of ~4-8 km (Randel et al., 2021; Randel and Wu, 2005), are a prominent feature of the tropical
- 191 temperature and wind fields. This presents a potential for spectral overlap with the longer vertical wavelength portion of the
- 192 GW spectrum that this study aims to capture.
- 193 Several methods exist for background state determination and large-scale process separation. These broadly fall into two
- 194 categories: Vertical Detrending (VD), often applied to single profiles from instruments like lidars and radiosondes (Gubenko
- 195 et al., 2012; Khaykin et al., 2015), and Horizontal Detrending (HD). HD requires spatially resolved datasets like satellite
- 196 observations or model reanalyses and typically involves spatio-temporal averaging to define the background (Alexander et al.,

Ep magnitudes depending on the chosen method. 199 The choice of detrending method is particularly critical in the tropics due to the presence of waves like Kelvin waves. VD methods, if not carefully designed, may inadvertently remove GWs with long vertical wavelengths or, conversely, retain short 200 201 vertical wavelength components of planetary-scale waves (e.g., Kelvin waves observed with vertical wavelengths as short as 202 3 km, as noted by Alexander and Ortland., (2010) and Cao et al., (2022)). Consequently, Schmidt et al. (2016) strongly 203 recommend using HD for satellite data, as VD may overestimate GW activity by including remnant signals from synoptic and 204 planetary waves that possess significant vertical structure in the tropics. Given these considerations, our study employs an HD 205 approach, calculating the background profile within a fixed spatio-temporal grid (20° longitude × 5° latitude over 7 days), 206 which we deem best suited for retrieving GW energy information from the Aeolus, GNSS-RO, and ERA5 datasets. 207 The separation of the wind or temperature profile into a background state and perturbations using HD is intended to isolate 208 fluctuations characteristic of gravity waves by filtering out larger-scale and slower-evolving processes like the mean 209 components of Rossby and Kelvin waves. This selection relies on the distinct scale and structural characteristics of GW 210 perturbations. However, the work by Randel et al., (2021) using dense COSMIC-2 RO data reveals further complexities. They 211 found that "residual" small-scale temperature variances (analogous to our perturbation fields) exhibit coherent maxima in the 212 longitudinal and vertical shear zones of large-scale Kelvin waves. This suggests that the local atmospheric environment shaped 213 by Kelvin waves, particularly variations in static stability (N2), can modulate the amplitude of smaller-scale variability, 214 potentially including GWs. Furthermore, the assimilation of Aeolus wind data itself has been shown to directly impact the 215 representation of vertically propagating Kelvin waves in numerical weather prediction models, especially in regions of strong 216 vertical wind shear (Žagar et al., 2021). This implies that Kelvin waves are indeed present in the Aeolus observations and that 217 their characteristics might differ from those in reanalyses not assimilating Aeolus data. 218 To further refine the isolation of GWs and address the potential aliasing from such equatorial waves, our HD approach is 219 combined with a vertical band-pass filter applied to the perturbation profiles. This filter targets vertical wavelengths between 220 1.5 km and 9 km. The lower limit is chosen based on the effective vertical resolution of the instruments (particularly Aeolus), 221 while the upper limit of 9 km is selected to be slightly above the typical dominant vertical wavelengths reported for Kelvin 222 waves in the UTLS, thereby further reducing their potential contribution. This combined HD and vertical filtering methodology 223 has been widely used for retrieving GW Ep from temperature data (Alexander et al., 2008b; Schmidt et al., 2008; Šácha et al., 224 2014; Khaykin et al., 2015), and the availability of Aeolus wind profiles allows us to apply a consistent approach for GW Ek. 225 Nevertheless, it is acknowledged that a perfect separation is difficult. The sharpest vertical gradients associated with Kelvin 226 waves, or localized enhancements of GW activity within Kelvin wave-modified environments as suggested by Randel et al., 227 (2021) might still contribute to the derived GW energy. The interpretation of our GW Ek and Ep must therefore consider this

2008b; Khaykin et al., 2015). A comparative study by John and Kumar., (2013) highlighted significant discrepancies in derived

197

228

229

The following section discusses the retrieval of GW kinetic energy, Ek. The retrieval faces challenges separating large scale

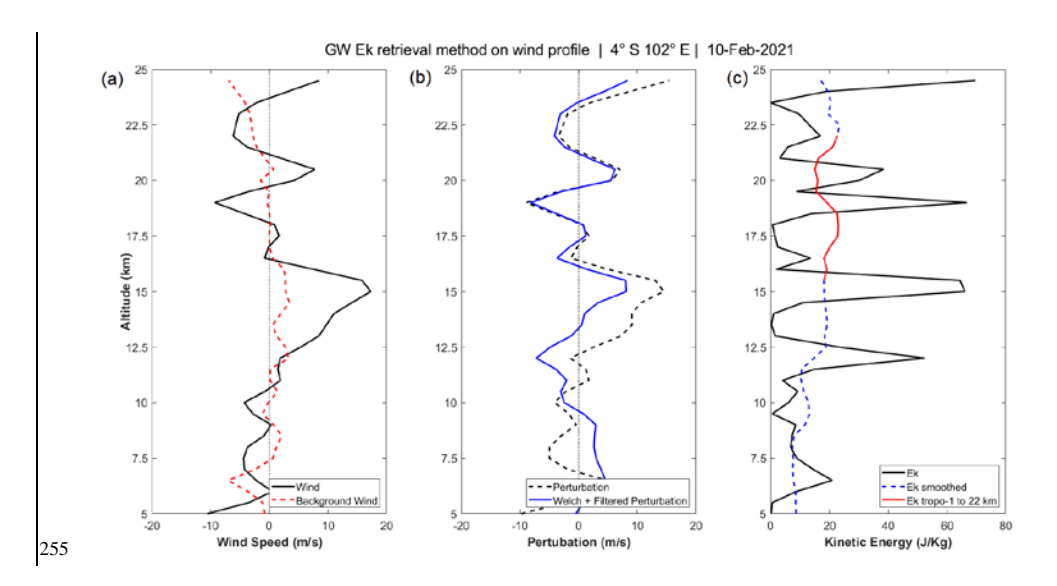
context, particularly when analyzing variability in regions known for strong equatorial wave activity.

processes, like gravity, Rossby, and Kelvin waves, from the smaller scale gravity waves.

Several methods exist for background state determination and large scale process separation, falling into two distinct categories: Either Vertical Detrending (VD), which can be applied to any type of data set, including local observations such as lidars and radiosondes (Gubenko et al., 2012; Khaykin et al., 2015) or Horizontal Detrending (HD), which also encompasses a temporal detrending component, requiring spatially resolved data set, i.e. satellite observations or model reanalysis (Alexander et al., 2008a; Khaykin et al., 2015). A study has discovered significant discrepancies in Ep magnitude when comparing different data sets using these methods (John and Kumar, 2013). Indeed, VD method may remove GWs with long vertical wavelengths whilst retaining short vertical wavelength planetary scale waves like Kelvin waves, which have been observed with vertical wavelengths as short as 3 km (Alexander and Ortland, 2010; Cao et al., 2022). Furthermore, Schmidt et al. (2016) strongly recommend using HD, as VD may overestimate gravity wave activity due to remnant signals from synoptic and planetary waves and their small vertical scale in the tropics. In our case, the method we propose (computation of background profile for a fixed spatiotemporal grid), falling into the HD category, is best suited for retrieving energy information from Aeolus and ERA5 model reanalysis.

The separation of the wind profile into a background state and perturbations through HD focuses on scales characteristic of gravity waves, thereby filtering out larger-scale processes like Kelvin and Rossby waves. This selection criterion is based on both the scale and structural characteristics of the perturbations. The frequency and wavelength of these perturbations are also critical identifiers of gravity waves, distinguishing them from other atmospheric phenomena.

Moreover, our approach utilizes high pass filtering techniques, targeting specific frequency or vertical wavelength ranges (7km in Alexander et al. (2008b) and 9km in this study), to further ensure that the perturbations derived from the background profile predominantly represent gravity waves. This method has been widely used for retrieval of GW Ep (Alexander et al., 2008a; Schmidt et al., 2008; Šácha et al., 2014; Khaykin et al., 2015), and Acolus now provides the necessary tools to apply the same approach for GW Ek.



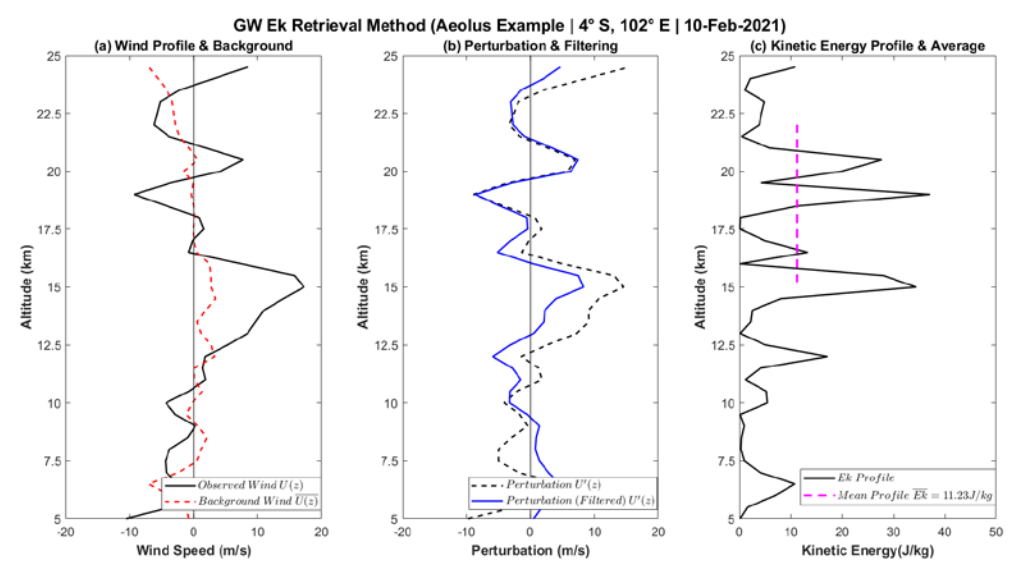


Figure 1. Derivation of GW energy profiles from wind measurements (a) Observed wind profile and the corresponding background state profile. (b) Wind perturbation profile alongside its filtered counterpart. (c) Resulting in Ek, smoothed and then averaged within the given altitude range.

Based on the linear theory of GW, the measured wind profile U(z) shown in Fig.1a is divided into a background wind $\overline{U}(z)$

also present in Fig. 1a and a perturbation U'(z) depicted in Fig. 1b. The background is obtained by averaging all individual wind 260 261 profiles for kinetic energy retrieval, within a spatiotemporal grid box of 20° longitude × 5° latitude over 7 days. While this 262 horizontal detrending method was originally demonstrated using temperature profiles in Alexander et al., (2008b), its 263 application to wind profiles is theoretically sound. Linear gravity wave theory dictates that wind and temperature perturbations 264 are coupled manifestations of the same wave phenomena, and thus the principle of separating smaller-scale waves from the 265 large-scale background flow via spatiotemporal averaging is equally valid for both fields. Following the arguments presented 266 in Alexander et al., (2008b), this choice is justified by the need to ensure a sufficient number of profiles per grid cell, which 267 minimizes random noise while preserving meaningful variability in the data. Shorter temporal windows would lead to 268 insufficient sampling, while longer windows would smooth out critical small-scale wave features. The grid size is also designed to preserve the spatiotemporal variability of mesoscale gravity waves and equatorially trapped structures, in an attempt 7 269

270 making it possible to separate the background and perturbation components without introducing significant biases.

Finally, this configuration mitigates errors in the definition of the $\overline{U}(z)$ profile, ensuring reliable kinetic energy calculations and robust separation of gravity wave perturbations. We performed sensitivity tests with varying grid sizes and temporal windows to confirm that this configuration provides the best possible background state when prioritizing Aeolus retrieval (see Fig. A1 in Appendix A).—The average number of profiles used for the background state determination is 55 for Aeolus, 20 for GNSS-RO and 1400 for ERA5.

276 GNSS-RO and 1400 for ERA5277

259

271 272

273

274

275

289

278 The next step involves subtracting the background profile from its corresponding individual profile, eliminating most large-279 scale waves (Planetary Waves, Kelvin Waves, Rossby Waves). This yields the perturbation profile U'(z), which is then 280 subjected to Welch-windowing, which is done in order to mitigate spectral leakage (Alexander et al., 2008a; 2008b; Khaykin 281 et al., 2015). A prior study also applied a similar windowing function (half cosine), aiming to counteract the "effects of the edge of the height range" (Hei et al., 2008). After said windowing, a band-pass filter designed to retain vertical wavelengths 282 283 between 1.5 km and 9 km. is applied to the perturbation profile, as seen in Fig.1b and 1c. The upper limit of 9 km isolates 284 GWs from larger-scale planetary waves, consistent with our background removal strategy. The lower limit of 1.5 km is chosen 285 to reflect the effective vertical resolution of the Aeolus instrument (Ratynski et al., 2023) and ensures that our comparison is 286 restricted to wave scales reliably resolved by all datasets (Banyard et al., 2021). This procedure provides a methodologically 287 consistent basis for comparing GW energy across the different instruments. After said windowing, a vertical high pass filter with a cut-off at 9 km is applied to the perturbation profile, as seen in Fig.1b and 1c. 288

290 The highpass filtering is a step that could be considered optional depending on the spectrum of waves studied. Short vertical scale waves in the tropical tropopause layer (TTL) region are particularly interesting due to their influences on thin cirrus and 291 292 stratospheric dehydration, and their potential role in driving the Quasi Biennial Oscillation (QBQ) in the lowermost 293 stratosphere (Kim and Alexander, 2015; Bramberger et al., 2022). Their smaller scale relative to larger atmospheric waves 294 justifies the use high pass filtering step and are the main cause for this choice.

295 The GW Ek can be derived from the variance of wind components as follows:

297

306 307

308

309

310

311

312

313

314

315

317

318

296
$$E_k = \frac{1}{2} \left(\overline{u'^2} + \overline{v'^2} + \overline{w'^2} \right),$$
 (2)

298 where u, v, and w represent the zonal, meridional, and vertical wind components, respectively. Considering that Aeolus's 299 viewing geometry in the tropics makes its HLOS wind primarily sensitive to the zonal component (as shown in Eq. 1), we will 300 note all mentions of retrieved speed as u for clarity. In our case, since the vertical wind speed is neglected and the satellite is 301 not able to distinguish between zonal and meridional wind, it is necessary to provide a new formalism for the retrieved metric: 302 where u, v, and w represent the zonal, meridional, and vertical wind components, respectively. However, in our case, since the 303 vertical wind speed is neglected and the satellite is not able to distinguish between zonal and meridional wind, it is necessary 304 to provide a new formalism for the retrieved metric:

$$305 E_{k HLOS} = \frac{1}{2} \left(\overline{uv'^2}_{HLOS} \right) (3)$$

The resulting profile, which is essentially the perturbation squared, is cut to keep the data between one kilometer below the tropopause and 22 km. The altitude range is chosen considering Aeolus' limitations, such as increasing error at higher altitudes due to lack of backscatter signal (Ratynski et al., 2023, their Fig.3). The lower bound is set one kilometer below the tropopause to focus on events extending beyond it, balancing Aeolus' resolution with our interest in upper-end dynamics. For consistency, the tropopause height is derived directly from the ERA5 dataset for all analyses. The profile is then averaged over the selected range, representing the Ek, as seen in Fig.1c. The tropopause is latitude dependent and determined using NCEP reanalysis, which provides results similar to ERA5 but is more accessible and easier to integrate. The profile is then smoothed using a 14point moving average over the 49-point profile and finally averaged over its total length, representing the Ek, as seen in Fig.1c.

316 We acknowledge that including the layer just below the tropopause presents a potential challenge, as strong, non-wave divergent outflow from deep convection could be partially aliased into our derived kinetic energy (Stephan et al., 2021). To rigorously test the robustness of our results against this potential contamination, we have performed a comprehensive

319 sensitivity analysis by recalculating the kinetic energy fields using two more conservative averaging layers, starting from 1 320 km and 2 km above the tropopause, respectively (see Fig.B1 and B2 in Appendix B). The detailed results of this analysis

321 confirm that our main conclusions are not sensitive to this choice. Mis en forme: ng-star-inserted, Justifié, Interligne: 1,5 ligne, Motif: Transparente (Blanc)

Although the above steps focus on retrieving GW Ek from Aeolus wind measurements, the same procedure can be applied to temperature-based observations such as GNSS-RO for Ep. The main difference lies in substituting temperature T(z) for wind U(z) throughout the background-perturbation decomposition, which means using T'(z) rather than U'(z). The Welch window was applied to all perturbation profiles (wind and temperature) before filtering to mitigate spectral leakage. The same band-pass filtering strategy and vertical averaging then provide the Ep profile from the temperature perturbations. The same low-pass and high pass filtering strategy, windowing (e.g., Welch or half cosine), and vertical averaging steps then provide the Ep profile from the temperature perturbations. In this case, the GW Ep is calculated using this formula:

$$E_p = \frac{1}{2} \left(\frac{g}{N}\right)^2 \left(\frac{T'}{\bar{T}}\right)^2 \tag{4}$$

Where the Brunt Vaisala frequency squared (N2) is smoothed using binomial (Gaussian) smoothing of 10th order.

Consequently, the data treatment across various instruments, whether wind or temperature remains consistent.

335 The E_{kHLOS} metric derived from Aeolus (Eq. 3) represents the kinetic energy projected onto the instrument's line of sight.
336 Since our study focuses on the tropical UTLS region, the meridional wind component will have a minor contribution compared
337 to the zonal component. Therefore, the E_{kHLOS} energy represents primarily the zonal activity, meaning that we are missing a
338 non-negligible proportion of wave activity. To evaluate the contribution of v' to the total kinetic energy we use ERA5 data
339 and compute the ratio between total Ek (derived from u' and v') and E_{kHLOS} (as it is observed by ALADIN).

This ratio (Fig. C1 in Appendix C1) exhibits significant geographic variability, which can be linked to physical mechanisms that create wave anisotropy. For instance, over regions like the Indian Ocean, the ratio is relatively low (~1.5), suggesting a predominantly zonal orientation of wave energy. This is physically plausible, as persistent surface winds like the trade winds can influence the tropopause-level wave field through two main processes. Firstly, flow over orography can preferentially generate zonally-oriented waves (Kruse et al., 2023). Secondly, the background wind profile itself acts as a directional filter, selectively allowing waves propagating in certain directions to reach the UTLS while attenuating others through critical-level interactions [Plougonven et al., 2017; Achatz et al., 2024].

When averaged over the mission period and focused on the equatorial band ($10^{\circ}\text{S}-10^{\circ}\text{N}$), the ratio settles at approximately 1.6. This implies that Ek_{HLOS} accounts for around 62.5% of total Ek, the remainder being undetectable due to HLOS projection. The meridional component, less significant in this specific geographical area for Aeolus, contributes the remaining 37.5% of Ek not considered by Ek_{HLOS} . Although not dominant, Ek_{HLOS} represent a substantial contribution to Ek. This scaling factor is used when discussing the implications of our Aeolus findings for the total GW kinetic energy budget. The details of the spatio-temporal variability of this ratio are provided in the Appendix C.

Code de champ modifié

Mis en forme : Anglais (Royaume-Uni)

Mis en forme: Anglais (Royaume-Uni)

Since our study focuses on the tropical UTLS region, the meridional wind component will have a minor contribution compared to the zonal component. Therefore, the $E_{k,RLOS}$ energy represents majorly the zonal activity, meaning that we are missing a non-negligible proportion of wave activity. To evaluate the contribution of v' to the total kinetic energy we use ERA5 data and compute the ratio between total Ek (derived from u' and v') and $E_{k,RLOS}$ (as it is observed by ALADIN).

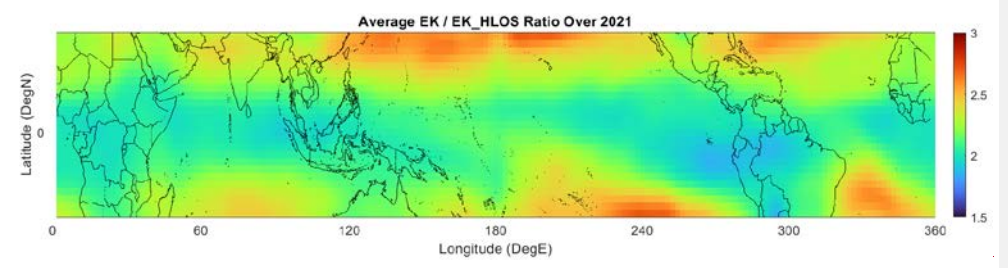


Figure 2. Temporal and spatial variability of the ratio between E_{kHLOS} and Ek in the ERA5 model over the tropical region (30°S–30°N) for the year 2021

Figure 2 displays the ratio between $E_{k,RLOS}$ and Ek in the ERA5 model, over the tropical region for the UTLS. The ratio values range from 1.5 to 3, between January 2021 and December 2021 included, depicting variations in how well the HLOS measurements capture the total kinetic energy in this region.

We specifically selected the year 2021, a period characterized by high energy levels in the Aeolus dataset. However, this choice does not significantly affect the spatial distribution of the ratio, as the overall patterns remain consistent year to year (the projection is always the same). By focusing on a single year, we aim to highlight the most prominent features of the ratio without averaging out key differences.

In general, the degradation of the Ek ratio as we move away from the equator is evident, aligning with theoretical expectations based on Eq. 1. For example, over the Indian Ocean, robust and persistent easterly trade winds align well with Aeolus' line-of sight direction, keeping the ratio relatively low at around 1.5. In contrast, over regions with more meridionally oriented circulations, such as parts of the American continent during certain periods, Aeolus captures less of the total kinetic energy due to the weaker zonal flow, pushing the ratio upward. Over the equatorial band (10°S 10°N), the ratio exhibits notable regional variations. In the western Pacific (120°E 180°E), the ratio remains relatively stable, fluctuating between 1.6 and 1.9 for this specific year, suggesting that a significant portion of the zonal wind energy is captured by Aeolus in this region. In contrast, over the American continent (240°E 300°E), the ratio increases significantly, reaching values up to 2.6, indicating a greater influence of the meridionally propagating GWs. Meanwhile, over the Indian Ocean (60°E 120°E), the ratio is lower,

around 1.5 to 1.6, implying that a larger fraction of the total kinetic energy is captured by Aeolus, due to the predominance of the zonal tropical trade winds in this region.

When these values are averaged over the years of the mission, the overall patterns remain similar, but with slightly different magnitudes. Over the western Pacific, the ratio tends to settles at 1.6, while the American continent displays a higher ratio, averaging closer to 2.8. The Indian Ocean shows the lowest ratios, typically around 1.5 in long-term averages, with the lowest values reaching as low as 1.2, further supporting the idea that the zonal wind predominance in this region allows Aeolus to capture a greater share of the total kinetic energy.

When averaged over the entire mission and focused on the equatorial band, the ratio settles at approximately 1.6. This implies that *Ek*_{HLOS} accounts for around 62.5% of total Ek, the remainder being undetectable due to HLOS projection. The meridional component, less significant in this specific geographical area for Aeolus, contributes the remaining 37.5% of Ek not considered by *Ek*_{HLOS}. Although not dominant, *Ek*_{HLOS} represent a substantial contribution to Ek.

The methods employed constrain the analysis to a specific range of horizontal and vertical wavelengths. Thanks to the given instruments and methods, we can predict both the horizontal and vertical wavelength range of the observations. Aeolus' RBS determines the spacing between sampling points, impacting the vertical and horizontal resolution and maximal detectable wavelength. The vertical wavelength analysis is constrained by the 9 km upper band-pass, representing. For vertical wavelengths, the maximum detectable limit with Aeolus is approximately 9 km, roughly half the average profile length in the tropics, after limiting the profile to the optimal range and especially considering the dynamic lower bound. Profiles generally extend to heights between 23km and 26km. The windowing function, along with the high pass filter, will also dampen the dominant wavelength. In the horizontal dimension, since a 20° x 5° degrees grid is used for the background removal and the wind is supposed quasi-zonal, the zonal wavelengths, therefore, reside below 2220 km.

Additionally, Aeolus can be prone to errors alternating the quality of wind profiles. Amongst the most notable ones are dark currents in the charge-coupled devices ("hot pixels"), potentially leading to errors of up to several meters per second (Weiler et al., 2021). Another identified issue is the oscillating perturbations, parasitic deformations of the signal, yet to be attributed to a cause, which can be mistaken for GW-induced signals (Ratynski et al., 2023). While corrections were implemented for the first issue (Weiler et al., 2021), the overall signal random error varies with time, with a general tendency to increase due to instrument degradation. Aeolus' HLOS wind variance is inherently linked to the measurement noise (i.e., random error). In other words, the observed wind variance is a sum of the variance due to waves (detected using the given data and method) and the variance due to ALADIN noise, i.e., its random error squared.

$$413 \quad \overline{uv'^2}_{HLOS} = \overline{uv'^2}_{GW} + \overline{uv'^2}_{LN}$$

$$414$$

$$(5)$$

with $\overline{u'^2}_{GW}$ representing the variance contribution from gravity waves and $\overline{u'^2}_{LN}$ the contribution from instrument noise. Since 415 kinetic energy is proportional to variance, this relationship holds for kinetic energy as well. The observed Aeolus kinetic energy 416 417 Ekaeolus HLOS is therefore the sum of the true geophysical signal and a noise component which increases over the mission 418 lifetime. To isolate the true gravity wave energy, this time-varying noise component must be estimated and removed. This 419 correction is performed at the kinetic energy level. While radiosondes provide a valuable independent reference, their sparse 420 coverage in the tropics makes them unsuitable for creating a globally consistent correction field. We therefore use the ERA5 421 reanalysis as a temporally stable global reference to estimate the Aeolus instrument noise. The core principle is to produce a 422 corrected dataset, denoted as $\overline{E}k_{Aeolus\,HLOS*}$ by subtracting our best estimate of the noise energy $\overline{E}k_{IN}$ from the observed 423 $\overline{Ek_{Aeolus\ HLOS*}} = \overline{Ek_{Aeolus\ HLOS}} - \overline{Ek_{J.N}}$ 424 (6) The estimation of the noise term, $\overline{Ek_{l,N}}$, is not a simple subtraction. It is derived using a spatio-temporally adaptive algorithm 425 426 that blends an additive offset (representing baseline instrument noise, dominant in quiescent atmospheric regions) with a 427 multiplicative scaling factor (more influential in active convective regions where noise effects might scale with the signal). 428 This adaptive approach ensures that instrumental artefacts are removed without suppressing the high-energy gravity wave 429 hotspots uniquely captured by Aeolus, or over-correcting areas of low variance. 430 An additional refinement step is required for seasonally averaged geographical maps. To produce these maps, individual profile 431 energy values were first binned into a 5° longitude by 2° latitude grid. A second stage adapts the noise correction derived from 432 the tropical 10°S-10°N band for application to the broader latitudinal extent of the maps (e.g., 30°S-30°N), accounting for 433 latitudinal variations in energy and ensuring physically consistent, non-negative results. To reduce noise and highlight large-434 scale patterns, a 3-point median filter followed by a 3-point moving average filter was applied sequentially in both the zonal 435 and meridional directions. 436 The full mathematical derivation of the adaptive estimation of $\overline{Ek_{LN}}$, the details of the map-specific refinement, and a series of diagnostic plots, including comparisons of Aeolus data before and after correction to validate the assumptions made, are 437 438 provided in the Appendix D. 439 440 441 with representing the variance contribution from gravity waves and contribution from instrument noise. The instrument-442 induced variance can be estimated using collocated reference measurements, which are very sparse and may lack

representativeness, or using global meteorological data independent of ALADIN, such as ERA5. The second method was chosen, as ERA5 allows reducing geo temporal biases compared to fixed sites. While the ALADIN random error exhibits

443

445 some variability across the tropics, observed fluctuations remain within approximately ±30% (Borne et al., 2024; Ratynski et 446 al., 2023). This degree of variability is considered acceptable, as the correction is applied as a zonal average, effectively 447 smoothing out localized deviations. Another important assumption is that ERA5's random error does not vary with time. These 448 calculations are realized within the 10°S-10°N latitude band. The defined meshing for the estimation is 3 weeks, meaning that 449 for each bin, a time averaging will be applied. The values are zonally averaged, which signifies that an average of longitudinal 450 values is calculated for each latitude bin, a process illustrated by placing a cap over the terms. With this, ERA5 can provide independent energy values and is, therefore, able also to estimate the instrument induced variance and its time evolution. 451 452 However, the estimations must be done in terms of Ek, as other metrics (such as wind or perturbation) cannot be linked between 453 both datasets: $\overline{Ek_{LN}} = \overline{Ek_{Aeolus HLOS}} - \overline{Ek_{ERAS HLOS}}$ 454 (6) 455 $\overline{Ek_{Aeolus\,HLOS}} = \frac{1}{2} \overline{v'^2_{HLOS}}$ 456 457 458 By subtracting the Ek instrument noise (being the mean difference between Acolus and ERA5 Eks for each bin), we impose 459 ERA5's average Ek values onto Aeolus' Ek, therefore only leaving the physical signal, with a stable value over the entire 460 461 $\overline{Ek_{Aeolus\ HLOS*}} = \overline{Ek_{Aeolus\ HLOS}} - \overline{Ek_{LN}}$ With Ekanalus HLOS Ek. The correction values fluctuated from 5 J/kg in 2018 and 462 463 2019 to between 10 J/kg and 17 J/kg for the rest of the period, peaking at 23 J/kg in November 2021. 464 One remark that can be made is that the ERA5 dataset is used to both calibrate Ek_{Aeotus HLOS} and as a comparison to 465 466 Ekanolus HITESE, which could be considered questionable. While it should, in principle, be better to use the derived noise 467 contribution from an earlier study (Ratynski et al., 2023), relying on a singular sounding site introduces geospatial biases 468 because of the absence of a global perspective. Applying a site specific correction to an entire longitudinal dataset might

compromise the integrity of the results. Furthermore, the idea of utilizing multiple-sounding sites is constrained by the limited

469

470

availability of such sites, especially in the tropics.

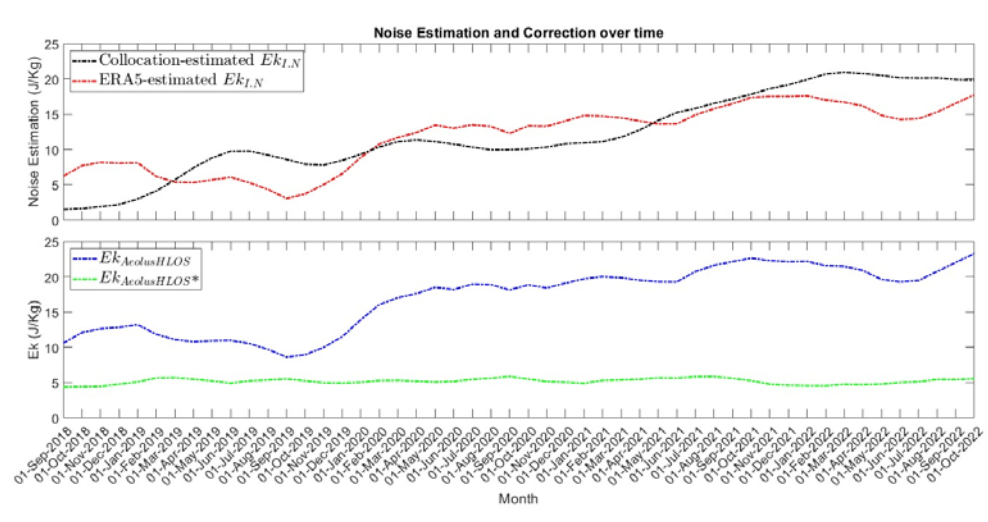


Figure 3. Difference between the Radiosonde-derived (black) and ERA5-derived (red) estimated noise correction, resulting in the difference between the uncorrected Acolus HLOS GW Ek (blue) and the ERA5-corrected Acolus HLOS GW Ek (green).

Figure 3, displaying both correction approaches (Site-based on top and model-based on the bottom), is intended to demonstrate that such a method of instrumental noise estimation is qualitatively consistent with the classical approach based on collocated reference measurements applied in (Ratynski et al., 2023).

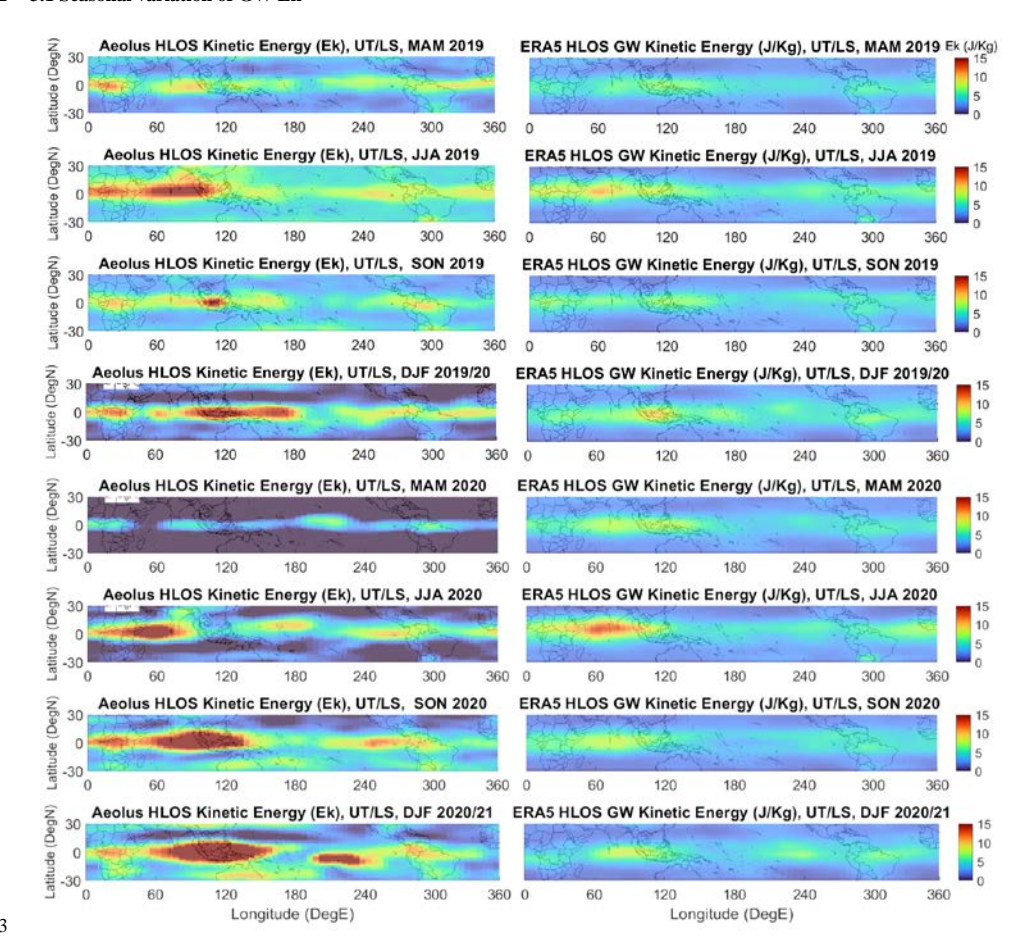
The Météo France upper air soundings in La Réunion (Aéroport Gillot) was used for the conduct of this analysis. For each collocated radiosonde profile with an Aeolus overpass (within 200 km and +/- 6 hours), we downsampled the radiosonde profile resolution to be equivalent to ALADIN vertical bins. A point wise difference is then calculated, and the standard deviation of these differences is what we refer to as random error. In principle, if Aeolus would not experience any degradation through its systems, this standard deviation would remain stable over the years and periods. However, since we observe an increase, as reported by Ratynski et al. (2023, their Fig.6), a link can be made between the instrument degradation and this increase, wrongly attributing signal to noise. Squaring this noise estimation provides a metric homogenous to the observed Ek, representing the repercussions of noise on Ek estimation:

$$Ek_{LN} = \frac{1}{2} \left(\sigma_{Aeolus-Radiosondes} \right)^2 \tag{9}$$

While both methods provide similar trends, the model approach remains the safest estimation when considering the potential biases.

3. Results

492 3.1 Seasonal variation of GW Ek



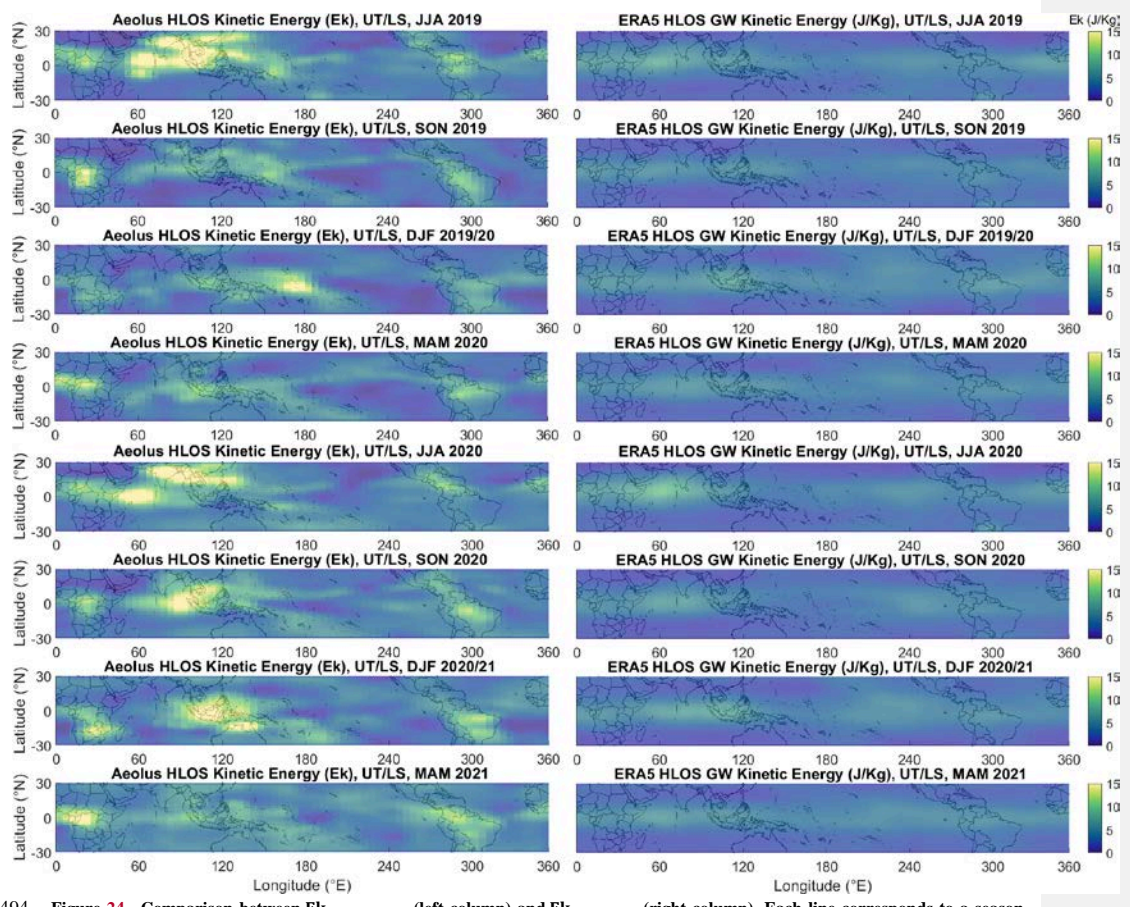


Figure 24. Comparison between Ek_{Aeolus HLOS}, (left column) and Ek_{ERA5 HLOS} (right column). Each line corresponds to a season, from June-July-August March-April-May 2019 to March-April-May December-January-February 2021. The white bins represent 496 the lack of satellite information. The UTLS altitudes are defined between one kilometer below the tropopause and 22 km. The 497 tropopause is determined from the ERA5NCEP reanalysis. The maps are smoothed using a combination of median and moving average filters as described in the Methods section.

495

498

499

500

Figure 2 displays the Ek_{HLOS} distribution from the Boreal Spring of 2019 to the Austral summer of 2020, derived from the corrected Aeolus observations and the ERA5 reanalysis. This comparison reveals both key similarities in large-scale patterns and significant differences in the representation of regional wave activity.

503 15°N). This observation aligns with the expectation that deep tropical convection, concentrated within the Intertropical 504 Convergence Zone (ITCZ), is a primary source of the observed waves. A clear seasonal cycle is evident in both Aeolus and 505 ERA5. During Boreal summer (JJA), enhanced Ek is prominent over Central Africa and the Indian Ocean. This corresponds 506 to the active phases of the African and Indian monsoon systems, which provide a persistent, large-scale environment favorable 507 for the development of organized, deep convective systems known to be efficient gravity wave generators (Forbes et al., 2022). 508 During Boreal winter (DJF), the focus of activity shifts eastward towards the Maritime Continent and the Western Pacific, 509 coinciding with that region's primary convective season. These general patterns are also consistent with previous climatologies 510 of GW potential energy derived from temperature measurements Alexander et al. (2008b, their Fig.3 and Fig.4). The GNSS-511 RO derived Ep values, which range from 0 to 6.6 J/kg at 15 km and 0 to 4.4 J/kg at 22 km (Alexander et al., 2008d), after 512 applying the usual Ek/Ep ratio of 1.6, are generally aligned with our observations. 513 514 It is also necessary to clarify the interpretation of the wave activity observed at the subtropical edges of our analysis domain 515 (near 30°N/S). While our study focuses on convectively generated waves originating from the deep tropics, the kinetic energy 516 measured in the subtropics is likely dominated by different, local sources. The strong subtropical jets and associated frontal 517 systems are potent generators of inertia-gravity waves through mechanisms of geostrophic adjustment and shear instability 518 (Kruse et al., 2023; Plougonven and Zhang, 2014). A recent case study has confirmed that such jet-merging events can produce 519 significant, large-scale GW fields (Woiwode et al., 2023). These jet- and front-generated waves typically have sub-weekly 520 periods and significant wind perturbations, meaning they fall within the detection window of our filtering methodology (Achatz 521 et al., 2024). Therefore, the enhanced energy often visible near 30°N and 30°S in our seasonal maps should be interpreted as 522 stemming primarily from these midlatitude dynamical processes, rather than from the poleward propagation of the equatorial 523 convective waves. 524 Despite these general agreements, a critical difference emerges in the structure and intensity of the energy hotspots. ERA5 525 tends to represent GW activity as a relatively smooth, zonally elongated band, with modest seasonal modulation. In stark 526 contrast, Aeolus reveals a picture of much more localized and intense Ek hotspots. For example, during JJA 2020 and SON 527 2020, Aeolus observes a well-defined hotspot over the Indian Ocean with Ek values exceeding 10-12 J/kg, whereas ERA5 528 shows only a diffuse enhancement in the same region with values rarely exceeding 5-7 J/kg. Similarly, the DJF 2020/21 hotspot 529 over the Maritime Continent is markedly stronger and more geographically confined in the Aeolus data. 530 This discrepancy suggests that while ERA5 captures the broad climatic envelope of convective GW activity, it significantly 531 underestimates the peak energy of waves generated by localized, intense convective systems. This is particularly evident in 532 regions where conventional wind observations are sparse, such as the Indian Ocean. The direct wind profiles from Aeolus 533 appear to capture magnitudes and structures of this convection-driven wave activity that are not present in the reanalysis.

Both datasets consistently show that the majority of GW kinetic energy is confined to the equatorial belt (approximately 15°S-

The period from mid-2020 onward, which coincided with the development of La Niña conditions, exhibits the most 535 pronounced differences between the two datasets. While La Niña is known to enhance convection over the Maritime Continent, 536 the consistently higher energy levels observed by Aeolus across all regions during this period also correlate with a documented 537 increase in the satellite's instrumental random error (Ratynski et al., 2023, their Fig.6). Our adaptive noise correction (see 538 Appendix D) is designed to account for this degradation. However, it is challenging to perfectly disentangle the increased 539 geophysical signal (e.g., from La Niña) from the effects of increased instrument noise. Nevertheless, the geographical 540 consistency of the hotspots observed by Aeolus, which align with known convective centers, provides confidence that the 541 primary patterns represent true atmospheric phenomena that are underrepresented in the reanalysis. 542 Finally, regarding the strong latitudinal confinement of the signal, while this is primarily a physical feature, our noise-543 correction methodology may also contribute to it. As detailed in the Appendix D (Part 2, step 2), the correction is weighted by 544 the latitudinal structure of the raw signal. This approach, designed to avoid over-correction in low-signal subtropical regions, 545 naturally sharpens the latitudinal gradient at the edges of the tropical belt. 546 Figure 4 displays the Ek_{HLOS} distribution from the Boreal Spring of 2019 to the Austral summer of 2020. This represents the 547 first attempt at an observation-based distribution of Ek from GWs in the tropics. From both Acolus and ERA5 points of view, 548 several recurrent and other dynamical spots can be observed. A notable hotspot over the Indian Ocean in JJA likely relates to 549 Indian Monsoon convection, dissipating by SON. This region is known to have frequent convective events generating many 550 GW activity (Holloway and Neelin, 2007).In DJF, a new hotspot is seen over the Western Pacific and Maritime Continent. 551 There is year round increased activity over the African continent, probably due to continental convection and higher than 552 average values over the Maritime Continent. More generally, the exhibited Ek activity predominantly lies within the 10° N/10° 553 S boundary. Aeolus's alignment with ERA5 is notable, not only in terms of value but also in distribution and evolution. 554 Furthermore, a previous study using Ep have reported observations similar to ours: the patterns resemble the findings from 555 Alexander et al. (2008b, their Fig.3 and Fig.4), highlighting the same locations and general hotspot distribution. The GNSS-556 RO derived Ep values, which range from 0 to 6.6 J/kg at 15 km and 0 to 4.4 J/kg at 22 km (Alexander et al., 2008c), after 557 applying the usual Ek/Ep ratio of 1.6, are closely aligned with our observations. This study is independent regarding the 558 datasets and metrics analyzed, adding another layer of confidence. 559 560 In contrast to the earlier period, the comparison between Ekaeolus HLOS+ and Ekeras HLOS from March 2020 to February 2021 561 presents a significant deviation. This is a period of time when La Nina conditions developed, particularly for the SON to DJF 562 period in 2020, leading to increased precipitation in the Maritime Continent region. This climatic phenomenon can partially 563 explain the observed differences between the 2019 and 2020 data for these seasons. A noticeable disparity arises in the energy

534

564

levels, with Aeolus consistently exhibiting a greater degree of energy compared to ERA5. This discrepancy is not limited to

are largely similar between the two datasets; however, the intensity and scale of these hotspots are invariably higher in Aeolus. In JJA, the hotspot over the Indian Ocean previously seen in both Aeolus and ERA5 becomes more pronounced in the Aeolus data, while ERA5 shows a considerable reduction. By SON and DJF, the disparity reaches its peak, the energy in Aeolus remains high, with the hotspot over the Indian Ocean and Maritime Continent becoming even more pronounced. Despite the same general pattern in ERA5, the energy level is notably lower. Starting from DJF 2019/2020, a marked difference is observed between hotspots and other areas. This period coincides with a notable increase in the satellite's random error (Ratynski et al., 2023, their Fig.6), impacting the noise correction approach and leading to an overestimation of variations in high variability regions, while minimally affecting low variability areas. Consequently, this translates into altered background levels in the dataset. These observations underline a stark contrast between both datasets, in which Aeolus demonstrates a consistently higher level of energy. One prominent constant across all periods is the high energy activity over the African continent. This feature remains consistent regardless of the season or the year, implying a persistent mechanism likely associated with the continental convection processes that are typical for this region. The other hotspots, however, display more variability. While they maintain their general locations across different seasons, the intensity of energy at these hotspots is subject to significant changes. This variability is likely coming from the decreased quality in the Aeolus data and does not represent any physical change in the regime. This suggests a strong temporal consistency in the general structure of the energy distribution

specific seasonal dynamics but pervades across the entire year. The geographical distribution and evolution of energy hotspots

565

566 567 568

569

570

571

572

573

574

575

576

577 578

579

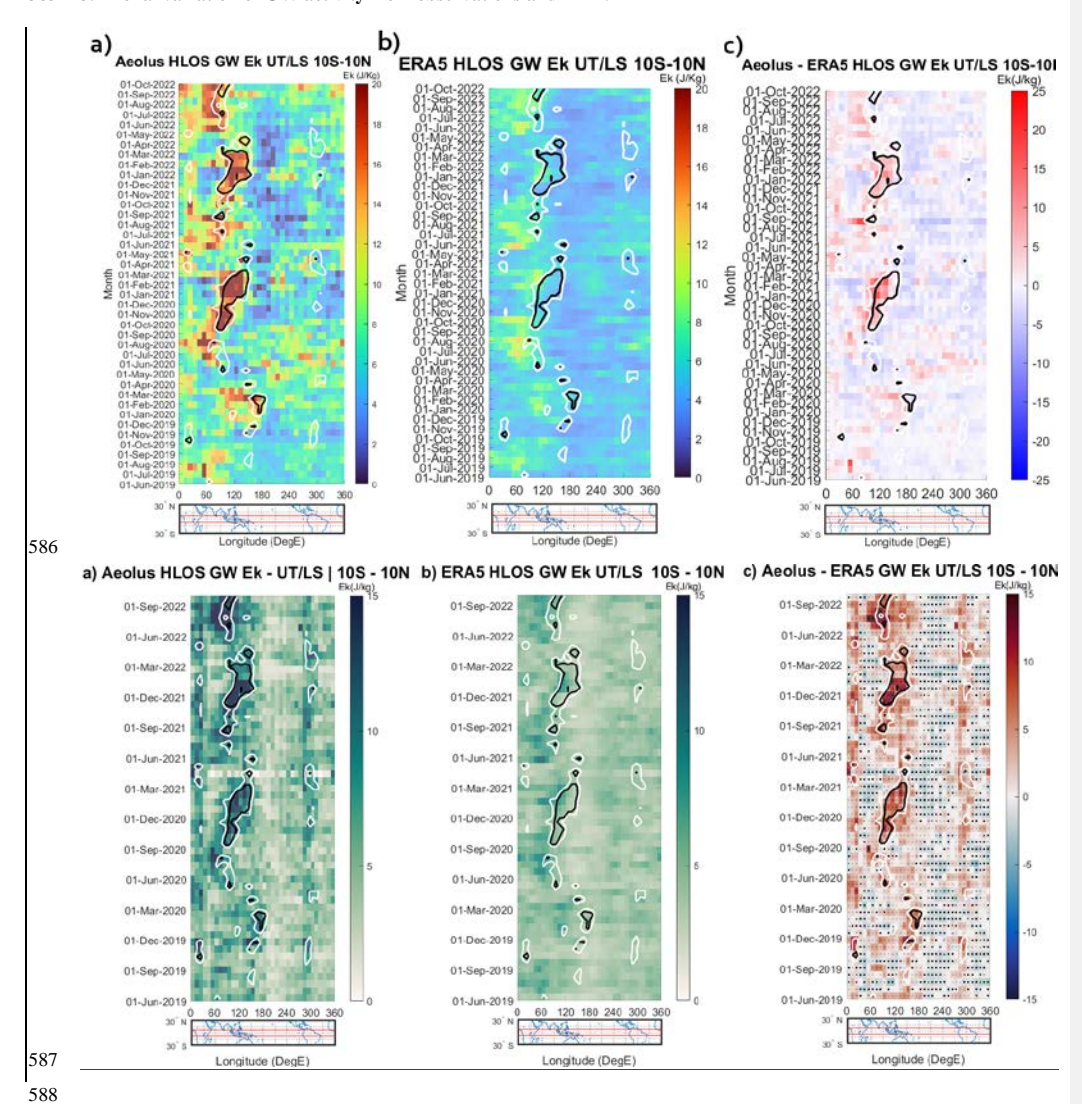
580

581

582

583

585 3.2 Zonal variation of GW activity from observations and ERA5



593 The tropopause is determined from the NCEP-ERA5 reanalysis. Black stippling indicates regions where the difference between 594 quantities is statistically significant (two-sample t-test, p < 0.05). 595 596 To assess the evolution and transition between the different seasons with greater precision, the Hovmoller diagrams in Fig.35 597 only show the observations within the deep tropics between 10° N and 10° S, as Fig.4 proves this region contains most of the 598 activity. Fig. 35a shows Ek_{Aeolus HLOS*}, where prominent hotspots of high Ek (often attaining 15 J/kg) are visible, with a broad 599 region of enhanced activity migrating eastward from the African continent (~0-60°E) towards the Indian Ocean and Maritime 600 Continent (~60-150°E) between June and March. This shift is recurring over multiple years and shows a relative consistency 601 between each year in terms of longitudinal and temporal range. 602 a recurrent eastward propagation is seen multiple times above the Indian Ocean. This hotspot migrates from eastern Africa to 603 the Pacific maritime continent between June and March. This shift is recurring over multiple years and shows a relative 604 consistency between each year in terms of longitudinal and temporal range. 605 606 The presence of hotspots, represented by distinct shapes in the Ek patterns, is expected in regions with prevalent convective 607 activity. These can be attributed to multiple powerful wave generation mechanisms occurring at the scale of individual storms. 608 One primary mechanism is thermal forcing, where the pulsatile nature of latent heat release in a convective updraft acts like a 609 piston on the surrounding stable air, generating a broad spectrum of gravity waves (Beres et al., 2005). A second, 610 complementary mechanism is mechanical forcing, where the body of the strong updraft itself acts as a physical barrier to the 611 background wind. The flow forced over this "moving mountain" generates large-amplitude, low-phase-speed waves that are 612 stationary relative to the storm (Corcos et al., 2025; Wright et al., 2023). The intense kinetic energy observed by Aeolus is 613 likely the signature of both mechanisms operating within active convective systems. These can be attributed to mechanisms

Figure 35. (a,b,c) Hovmoller diagram of Ek_{Aeolus HLOS}, Ek_{ERA5 HLOS} and their difference. The contour plot represents the Outgoing Longrange Radiation (OLR) for 210 and 220 W/m² (black and white, respectively). Each bin corresponds to an average of over 3

weeks and 10 degrees. The dark bins represent the lack of satellite information in (a). The OLR measurements were obtained from the Australian Bureau of Meteorology. The UTLS altitudes are defined between one kilometer below the tropopause and 22 km.

589

591

614

615

616 617

618

619

620

621

622

remains below 7 J/kg.

Code de champ modifié

responsible for convection induced GWs. Deep convection in the atmosphere produces localized regions of intense upward

motion and latent heat release. These convectively generated GWs can propagate vertically and interact with the large-scale

In sharp contrast, Fig.3b presents a much more subdued and less dynamic picture for the corresponding ERA5 perspective.

While ERA5 shows some broad, low-amplitude enhancement of Ek that co-locates weakly with the seasonal convective cycle,

it completely fails to capture the intense, high-energy hotspots observed by Aeolus. The organized eastward propagation and

the high peak energy values are entirely absent in the reanalysis. For nearly all regions and time periods, the Ek in ERA5

atmospheric circulation, transferring momentum and energy to the background flow (Alexander et al., 2021).

623 The difference between the two datasets, shown in Fig.3c, quantifies this discrepancy. The plot is overwhelmingly positive, 624 indicating a systematic and significant underestimation of GW kinetic energy by ERA5 throughout the tropics. The regions of 625 greatest underestimation, where the difference exceeds 10 J/kg, align almost perfectly with areas of deep convection, as 626 identified by the low Outgoing Longwave Radiation (OLR) contours. The OLR represents the amount of terrestrial radiation 627 released into space and, by extension, the amount of cloud cover and water vapor that intercepts that radiation in the 628 atmosphere. It is a widely used and reliable proxy for deep convection due to its strong correlation with diabatic heating (Zhang 629 et al., 2017), reinforcing the conclusion that ERA5's primary weakness lies in representing convection-driven wave activity. 630 To confirm the robustness of this finding, a two-sample t-test was performed for each grid cell. The stippling in Fig.3c indicates 631 where the mean Ek from Aeolus is statistically significantly higher than that of ERA5 (p < 0.05). The pervasive stippling 632 across nearly all convective hotspots underscores that the observed differences are not random fluctuations but represent a 633 fundamental deficiency in the reanalysis. This finding suggests that without the assimilation of direct, high-resolution wind 634 profile data like that from Aeolus, reanalysis models may not fully resolve the kinetic energy associated with gravity waves 635 generated by localized, intense convective events. An alternative display of Fig.3c as a ratio, along with an F-test, can be found 636 in Appendix E. 637 We observe similar spatial and temporal patterns between Ekacolus HLOSA and the Ekacolus HLOSA shown in Fig. 5b, with increased 638 Ek values corresponding to low Outgoing Longwave Radiation (OLR) areas. The OLR represents the amount of terrestrial 639 radiation released into space and, by extension, the amount of cloud cover and water vapor that intercepts that radiation in the 640 atmosphere. Based on the findings in the study by Zhang et al. (2017), OLR serves as a reliable proxy for deep convection due 641 to its strong correlation with diabatic heating and radiative tendencies. Hence, the correspondence between increased Ek values 642 and OLR contours is unsurprising. 643 644 While the Aeolus and ERA5 Ek variations are generally consistent, the datasets show some discrepancies. In particular, as can 645 be inferred from Fig.5c, ERA5 underestimates Ek in the regions of deep convection, characterized by lower OLR, suggesting 646 a possible weakness of the reanalysis in resolving convection induced wave activity. 647

Mis en forme : Anglais (Royaume-Uni)

4.1 Comparison with Potential EnergyWhile a conservative analysis might prioritize directly comparable metrics,

exploring less conventional approaches can reveal patterns that remain hidden in traditional frameworks. A key goal of this

study is to compare the kinetic energy from Aeolus with potential energy, the most common metric for GW climatologies.

4. Comparison with Potential Energy: possibilities and limitations Exploratory possibilities and limitations

However, this comparison is complicated by the longstanding assumption of a constant Ek/Ep ratio.

648

649 650

651

Traditionally, linear gravity wave theory proposes a near-constant ratio of Ek to Ep, often quoted between 5/3 and 2.0 (Hei et al., 2008; VanZandt, 1985). In stable, linear wave conditions, these theoretical predictions hold reasonably well (Nastrom et al., 2000). However, a growing body of evidence from empirical studies reveals significant variability in this ratio, suggesting that real-world atmospheric conditions often involve non-linear processes such as wave breaking or saturation, which are not accounted for in the linear theory (Baumgarten et al., 2015; Guharay et al., 2010; Tsuda et al., 2004).

ERA5 EK/EP UT/LS 10S-10N

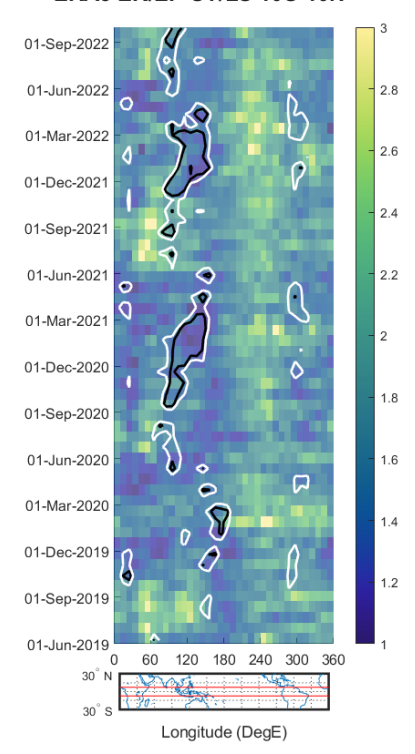


Figure 4. Spatiotemporal distribution of the Ek/Ep ratio in the ERA5 reanalysis for the equatorial band (10°S-10°N). The UTLS altitudes are defined between one kilometer below the tropopause and 22 km. The contour plot represents the Outgoing Longrange Radiation (OLR) for 210 and 220 W/m² (black and white, respectively). Each bin corresponds to an average of over 3 weeks and 10 degrees. The OLR measurements were obtained from the Australian Bureau of Meteorology. The tropopause is determined from the ERA5 reanalysis.

Mis en forme : Normal, Centré

665 ERA5 reanalysis. Figure 6 presents the longitudinal and temporal variations of this ratio in the equatorial UTLS. The figure 666 immediately reveals that the ratio is far from constant. It exhibits significant spatial and temporal variability, with values 667 frequently exceeding the linear theory predictions (>2). Notably, distinct hotspots of high Ek/Ep ratios are present, particularly 668 over the Indian Ocean at around 70° and the Western Pacific at 300°. In regions outside of the most intense convective activity, where ERA5 does manage to represent some kinetic energy 669 670 enhancement, the agreement with Aeolus is often satisfactory. This is visible in Fig. 5c, where the same areas (60° and 240°) 671 show a correct correspondence. This suggests that when wave generation is not dominated by deep convection, ERA5 can 672 reproduce realistic GW structures. The strong agreement in these non-convective regions also reinforces the idea that the 673 dominant winds have a strong zonal component, as the quasi-zonal u_{HIOS} measurement from Aeolus is sufficient to capture 674 these features. The elongated white stripe in Fig. 8a during February-March 2020 comes from an intense intraseasonal 675 disturbance, the 2020 Madden-Julian Oscillations (MJO), which can inject unusually strong gravity-wave energy into the upper 676 troposphere (Kumari et al., 2021). 677 The divergence between ERA5 and Aeolus becomes most pronounced precisely in the deep convective regions where Aeolus 678 observes its strongest Ek signals, inside the areas of low OLR. The discrepancy appears specifically linked to convection-679 driven dynamics, which are either not properly represented or fail to trigger sufficient wave activity within the ERA5 model's 680 parameterizations. This suggests that the primary cause of ERA5's underestimation is not a simple mispartitioning between 681 the horizontal wind components (i.e., a directional bias in the line-of-sight projection) but rather a more fundamental, large-682 scale underestimation of the total kinetic energy. 683 This model-internal result demonstrates that relying on a fixed ratio to infer one energy component from another is likely to 684 be inaccurate, especially in dynamically active regions. The partitioning of energy between kinetic and potential forms is itself 685 a key diagnostic of wave dynamics that requires further observational constraints. 686 One promising possibility of this study in providing deeper context lies in comparing the kinetic energy of gravity waves 687 observed by Aeolus with the potential energy derived from GNSS-RO data. GNSS-RO provides high-resolution temperature 688 profiles that are used to estimate the potential energy of gravity waves. Previous studies that looked into GW climatology all 689 relied on these estimate to base their observations on, as it was the only global instrumentation available (Schmidt et al., 2008; 690 Alexander et al., 2008a; Šácha et al., 2014; Khaykin et al., 2015), Hence, we will adopt this method of comparison as well,

To illustrate this complexity within a self-consistent framework, we first examine the Ek/Ep ratio derived entirely from the

664

691

692

693

694

695

696

Code de champ modifié

Mis en forme : Français (France)

Mis en forme : Français (France)

Mis en forme : Anglais (Royaume-Uni)

While a conservative analysis might prioritize directly comparable metrics and cautious interpretations, exploring less

conventional approaches can reveal patterns and relationships that remain hidden in traditional frameworks. One promising





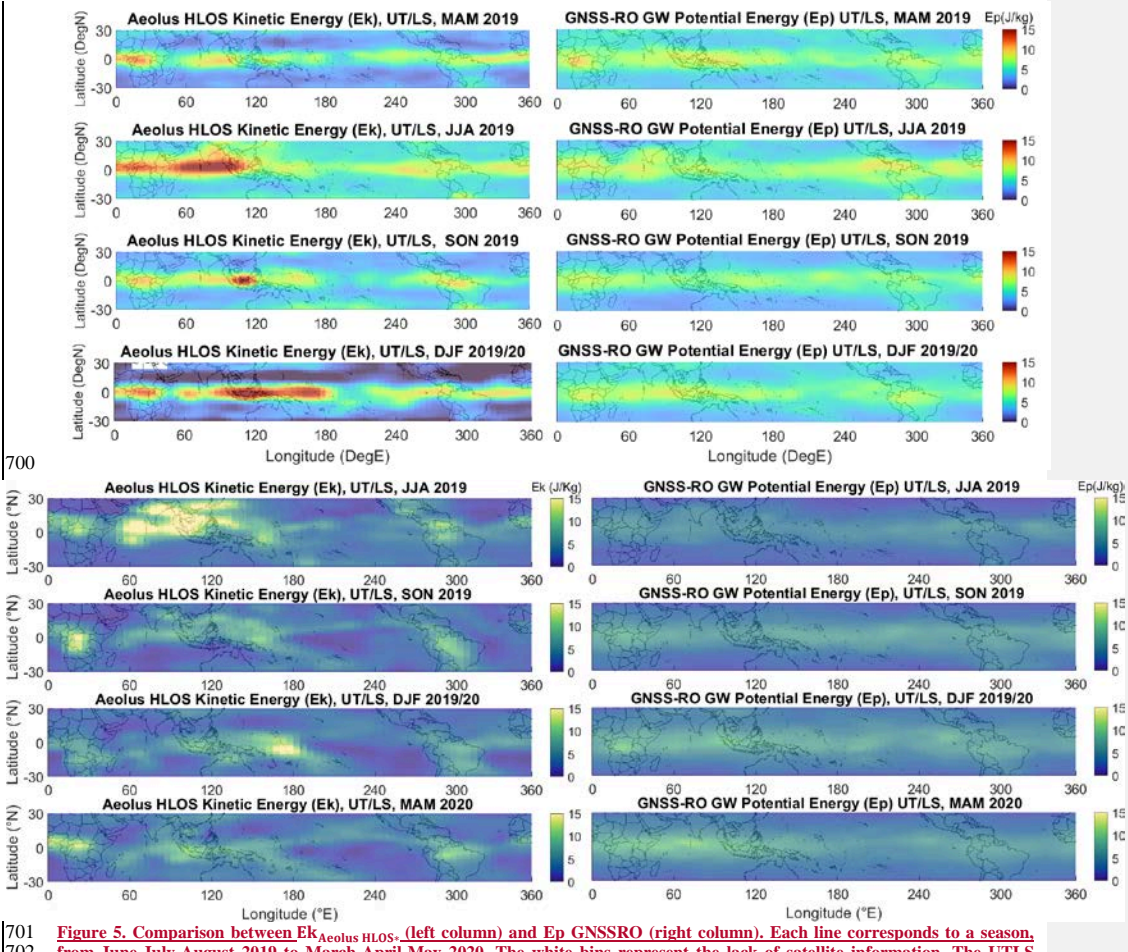


Figure 5. Comparison between Ek_{Aeolus HLOS}, (left column) and Ep GNSSRO (right column). Each line corresponds to a season, from June-July-August 2019 to March-April-May 2020. The white bins represent the lack of satellite information. The UTLS altitudes are defined between one kilometer below the tropopause and 22 km. The tropopause is determined from the ERAS reanalysis.

707 UTLS altitudes are defined between one kilometer below the tropopause and 22 km. The tropopause is determined from the NCEP 708 reanalysis. 709 Fig.56 offers a side-by-side seasonal comparison of EkAeolus HLOS* (left column) and Ep derived from GNSS-RO (right column), covering the period from March 2019 to February 2021. The figure highlights key spatial and temporal patterns of 710 711 gravity wave activity detected by each instrument, with both datasets presenting clear seasonal variability, 712 713 Although the ratios between Ek and Ep suggested by linear gravity wave theory generally range between 5/3 and 2.0, empirical 714 observations show significant variability. This variability, which is influenced by geographical factors, nonlinear processes, or 715 wave interactions, underscores the importance of examining these two forms of energy from different perspectives rather than 716 seeking strict correspondences. 717 718 With that in mind, what stands out from this comparison is the overall consistency in detecting gravity wave hotspots, 719 particularly within the tropical belt. One notable aspect of the comparison is the seasonal shift in gravity wave activity between 720 the two datasets, with both detecting enhanced wave activity during certain months. Because of inherent differences (different 721 line of sight and signal projection, different physical quantities and their varying ratio that is empirically challenging the 722 literature, different signal treatment and correction), direct one-to-one comparisons are not appropriate. Nonetheless, it allows 723 us to draw parallels with Aeolus observations, where spatial and temporal correlation of hotspots should follow the same disposition, allowing for an independent benchmark. Despite these methodological differences, both instruments align on the 724 725 seasonal peaks and general distribution of wave activity, reinforcing the reliability of the data.

726

Figure 6. Comparison between Ek_{Acolus HLOS}. (left column) and Ep GNSSRO (right column). Each line corresponds to a season, from March-April-May 2019 to December-January-February 2021. The white bins represent the lack of satellite information. The

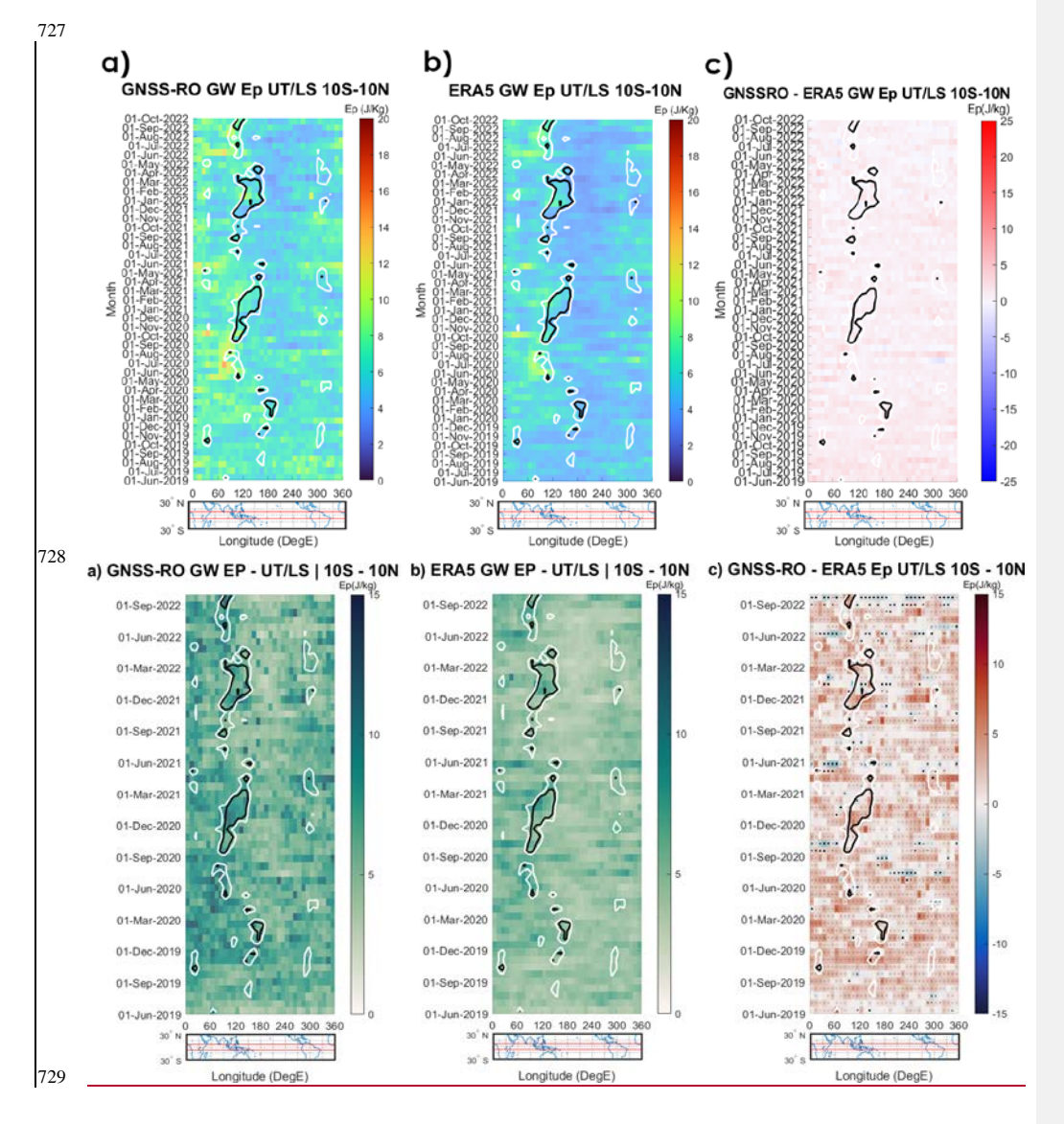


Figure 67. (a,b,c) Hovmoller diagram of Ep_{GNSS-RO}, Ep_{ERA5} and their difference. The contour plot represents the Outgoing Longrange Radiation (OLR) for 210 and 220 W/m² (black and white, respectively). Each bin corresponds to an average of over 3 weeks and 10 degrees. The OLR measurements were obtained from the Australian Bureau of Meteorology. The UTLS altitudes are defined between one kilometer below the tropopause and 22 km. The tropopause is determined from the NCEP_ERA5 reanalysis.

Black stippling indicates regions where the difference between quantities is statistically significant (two-sample t-test, p < 0.05).

|755

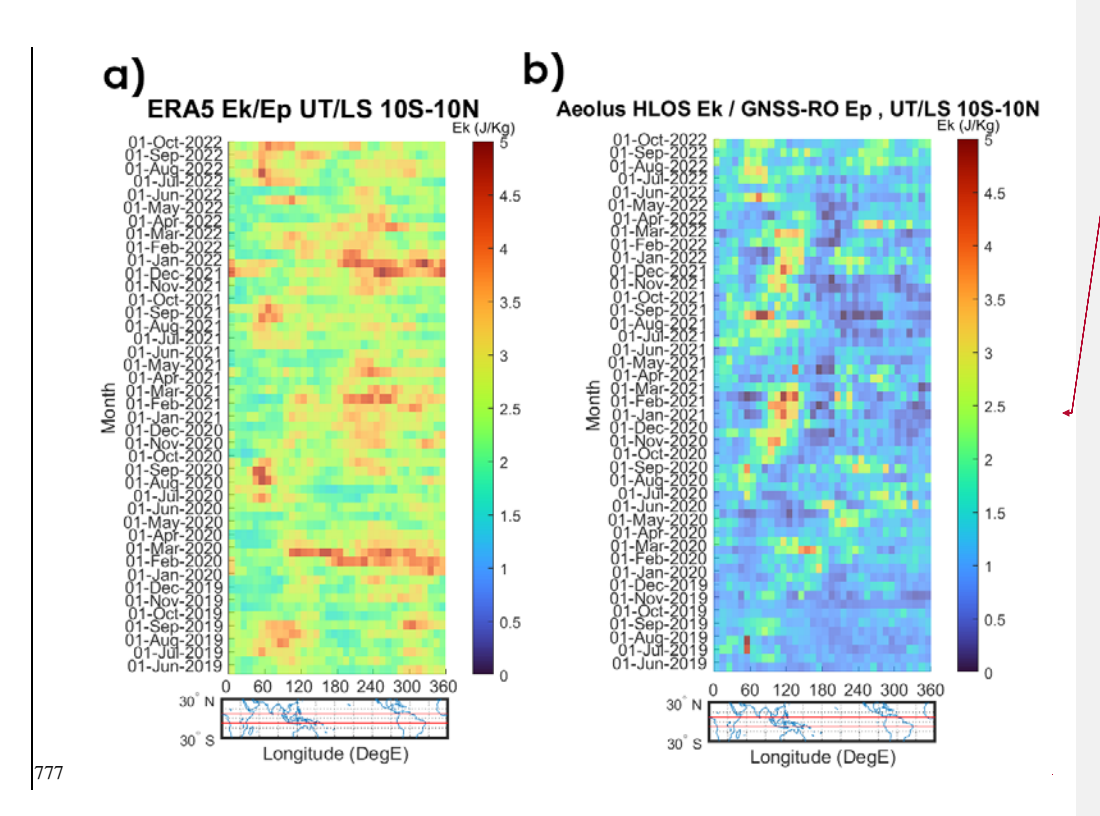
The Ep_{GNSS-RO} shown in Fig.67a does not perfectly align with the structures described earlier, nor does it closely follow the patterns of OLR activity. As the method employed removes any traces of kelvin waves in the signal, the remaining activity is only comprised of GWs. This suggests that Ep does not effectively capture GW activity in regions of deep convection, as indicated by the lowest OLR values. However, it is found that the lesser convective areas are seen both on instances of Ek and Ep, in Fig.5a and Fig.7a (with notable examples such as August 2020 around 100°E, as well as in May 2021 and 2022 near 50°E). This observation supports the notion that, in terms of GW activity, deep convective phenomena primarily generate Ek, while less intense convective events (indicated in Fig.7a as occurring in the neighbouring region outside the white contours) produce a more balanced distribution between both energy components. It would be incorrect to assume that no wave activity occurs in low OLR regions; previous studies have shown that Ep values peak at 15 km altitude around the maritime continent, where the Walker circulation rises under non-El Niño conditions (Ern et al., 2004; Yang et al., 2021).

Nonetheless, the Ep_{ERA5} diagram shown in Fig.67b is very consistent with the results shown in Fig.67a, particularly in regions outside the primary convection hotspots. For example, in August 2020 around 100°E, we see coherent signals in both datasets. Similarly, in May 2021 near 50°E or in February 2022 near 120°E, distinct patterns emerge in both datasets. These alignments indicate that when gravity waves have a stronger potential energy component, both datasets capture these features, even outside the primary zones of low OLR. It can also be noted that the patterns visible in Fig.7b strongly resemble the patterns presented by ERA5 in Fig.5b, a sign of ERA5's tendency to rely on the existence of Ep to determine the presence of Ek.

The differences between ERA5 and GNSS-RO data, depicted in Fig.7c, are minimal, with a mean absolute difference of approximately 1.5 J/kg. This close agreement is expected, given that ERA5 assimilates GNSS-RO temperature profiles. This result demonstrates that the reanalysis system successfully reproduces the observed potential energy field. This finding stands in sharp contrast to the significant underestimation of kinetic energy by ERA5 when compared to Aeolus observations (as shown in Fig 5c). The combination of these results (good agreement in assimilated Ep and poor agreement in unassimilated Ek) points to a specific limitation in the reanalysis's ability to model the kinetic component of convection-induced gravity waves, particularly in regions where direct wind observations are sparse.

An alternative display of Fig.6c as a ratio, along with an F-test, can be found in Appendix E.

The differences between ERA5 and GNSS-RO data, depicted in Fig.7c, are minimal and averaging at a 1.4 J/kg difference. Given that ERA5 assimilates GNSS-RO data, that conclusion does not come as surprising. While ERA5 accurately represents Ep in, and outside, of convective regions thanks to its assimilation of GNSS-RO data, the underestimation of Ek points to a specific limitation in capturing the kinetic energy component of convection-induced gravity waves. This discrepancy then results from the absence of data from Acolus or other instruments capable of retrieving similar wind-related information, as ERA5 mostly relies on geostrophic (thermal) winds in poorly wind assimilated areas. This reliance on derived wind data, rather than directly observed wind fields, could explain why ERA5 does not accurately capture the reality observed by specialized instruments like Aeolus, which directly measure actual wind components.



Mis en forme : Centré

Aeolus Ek / GNSS-RO Ep | UT/LS | 10S - 10N

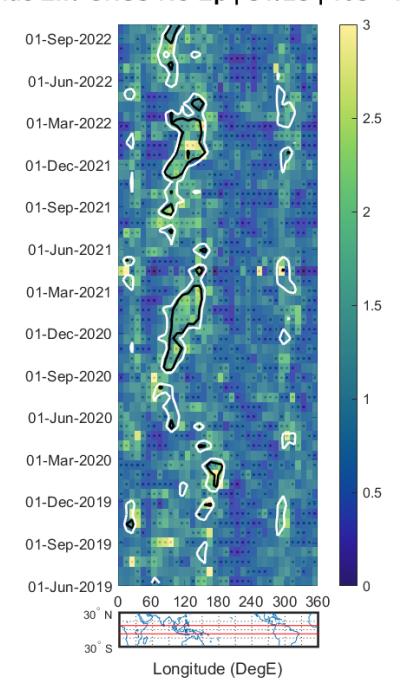


Figure 7. Relationship between Ek $_{\rm Acolus\,HLOS}$, and Ep from GNSSRO. The UTLS altitudes are defined between one kilometer below the tropopause and 22 km. The tropopause is determined from the ERA5 reanalysis. The tropopause is determined from the ERA5 reanalysis. Black stippling indicates regions where the difference between quantities is statistically significant (F-test, p < 0.05).

Figure 8. a) Relationship between Ek and Ep from the ERA5 point of view. b) Relationship between Ek_{Acolus HLOS}, and Ep from GNSSRO. The UTLS altitudes are defined between one kilometer below the tropopause and 22 km. The tropopause is determined from the NCEP reanalysis.

Fig. 7 presents the first observationally-derived long-term study of the Ek/Ep ratio, comparing Aeolus's HLOS Ek and GNSS-RO-derived Ep. It illustrates the longitudinal and temporal variations of the Ek/Ep ratio across the equatorial band (10°S to 10°N) from June 2019 to October 2022.

The regions with the highest ratio values are systematically co-located with areas of deep convection, as indicated by the low 791 OLR contours. This is particularly evident over the Indian Ocean (e.g., September-June 2019/20, 2020/21, and 2021/20) and 792 over the Western Pacific. This observation suggests that, in areas with similar seasonal characteristics, gravity waves tend to 793 transport more kinetic energy during convective events, which amplifies their influence on the overall energy dynamics. The 794 periodic patterns observed in the data also hint at a seasonal component previously observed by Zhang et al. (2010), potentially 795 tied to atmospheric phenomena such as the shifting ITCZ or changes in jet stream dynamics (Hei et al., 2008). These seasonal 796 fluctuations in the Ek/Ep ratio further reinforce the notion that gravity wave behavior is not static but is influenced by broader 797 atmospheric cycles (Ern et al., 2018; Zhang et al., 2010), contrary to the traditional linear theory paradigm in the literature. 798 Statistical significance testing (represented by the black stippling) confirms that these hotspots of high, convection-linked ratios are statistically significant features rather than artifacts. 800 A significant division between the Indian Ocean and the eastern Pacific, marked by a contrast around 200° longitude, can be 801 noted in both Fig.7 and Fig.4. This contrast reflects underlying geographic factors, including orographic influences and 802 convective activity. These two factors play a role in the generation and propagation of gravity waves, causing the distinct 803 variations in the ratio between the two energies. 804 This observational result stands in contrast to the picture presented by the ERA5 reanalysis in Fig.4. While ERA5 also shows 805 variability in its Ek/Ep ratio, its regions of highest ratio are often located outside the main convective centers. This suggests 806 that ERA5 misrepresents the physical link between deep convection and the partitioning of wave energy. 807 Given that ERA5 successfully assimilates GNSS-RO temperature data (and thus has a reasonable representation of Ep), this 808 discrepancy points to a fundamental difficulty in the reanalysis's ability to generate the corresponding kinetic energy 809 component in the right locations. Without direct wind profile assimilation in these data-sparse convective regions, the model's 810 parameterizations and background error covariances fail to create the intense, localized kinetic energy associated with 811 convective gravity waves. 812 However, it is noteworthy that in some specific regions and periods, such as over the Indian Ocean between June and 813 September of 2019, or in the longitude band around 300°E, a degree of correspondence between the model and observations 814 can be found. This suggests that for certain regimes, the reanalysis can approximate the energy partitioning, but it fails 815 systematically in the most intensely convective areas. These findings reinforce that direct kinetic energy measurements, as 816 provided by Aeolus, are essential for correcting model biases and improving our understanding of the gravity wave energy 817 budget.

818 Fig. 8 presents a detailed analysis of the ratio between Ek and Ep from two perspectives; (a) from the ERA5 model and (b) 819 comparing Aeolus's HLOS Ek and GNSS-RO-derived Ep. It illustrates the longitudinal and temporal variations of the Ek/Ep 820 ratio across the equatorial band (10°S to 10°N) from June 2019 to October 2022. When observed closely, a significant division between the Indian Ocean and the eastern Pacific, marked by a contrast around 821 822 480° longitude, can be noted in both figures. This contrast is not just a random occurrence but reflects underlying geographic 823 factors, including orographic influences and convective activity. These two factors play a role in the generation and propagation 824 of gravity waves, causing the distinct variations in the ratio between the two energies. 825 Figure 8a presents distinct hotspots in the Ek/Ep ratio, which could potentially arise from parametric noise or model 826 assumptions. However, the alignment of these hotspots in Fig.8b, as observed by Aeolus and GNSS-RO, two independent 827 instruments, (despite ERA5 assimilating GNSS-RO data) confirm the presence of these patterns. Notable examples include 828 the series of hotspots included on the 60° to 120° longitude (July to September 2019, July 2020 to March 2021, July 2021 to 829 March 2022 and July 2022 to October 2022) and another series of hotspots on the other side of the longitude range, at 200° to 830 260° longitude (February 2021 to March 2021 and December 2021 to March 2022). Since Aeolus provides energy metrics 831 through a specific line of sight, we can conclude that the western activity mostly provides from zonal winds (where both 832 patterns visually correspond), whereas the eastern activity probably contains a much stronger meridional component, 833 explaining the weaker visual fidelity. In particular, the large red stripe in Fig. 8a during February March 2020 comes from an 834 intense intraseasonal disturbance, the 2020 Madden-Julian Oscillations (MJO), which can inject unusually strong gravity-wave 835 energy into the upper troposphere (Kumari et al., 2021). The patterns on the western side of both figures show a pretty constant 836 seasonality, and it could be argued that this is also the case for the eastern side patterns. 837 Upon further examination of the correlation between areas of maximum Ek/Ep ratios and the presence of dynamic hotspots, 838 the data indicate a clear connection to regions of intense convective activity. This observation suggests that, in areas with 839 similar seasonal characteristics, gravity waves tend to transport more kinetic energy during convective events, which amplifies 840 their influence on the overall energy dynamics. The periodic patterns observed in the data also hint at a seasonal component 841 previously observed by Zhang et al. (2010), potentially tied to atmospheric phenomena such as the shifting Intertropical 842 Convergence Zone (ITCZ) or changes in jet stream dynamics (Hei et al., 2008). These seasonal fluctuations in the Ek/Ep ratio 843 further reinforce the notion that gravity wave behavior is not static but is influenced by broader atmospheric cycles (Ern et al., 844 2018; Zhang et al., 2010), contrary to the traditional linear theory paradigm in the literature.

Mis en forme : Normal, Espace Avant : Automatique, Après : Automatique

845

846 847 Understanding the vertical wavelength of convective GWs is an essential element for characterizing their dynamics. However,

Acolus is inherently limited in retrieving accurate vertical wavelengths due to its design. The placement of range bins was

848 fixed at the time of observation, introducing inconsistencies in vertical resolution that affect the precise identification of wave peaks and troughs. Additionally, the N/P parameter, which controls the number of accumulated measurements (N) and pulses (P) per cycle, introduces variability in the horizontal resolution of Aeolus data. Changes to this setting, such as the transition from N=30 to N=5, improve horizontal resolution but exacerbate the misrepresentation of vertical wave structures. These design limitations necessitate reliance on external datasets, such as ERA5, which provide a more continuous representation of vertical wave structures and finer-scale features.

849 850

851

852 853

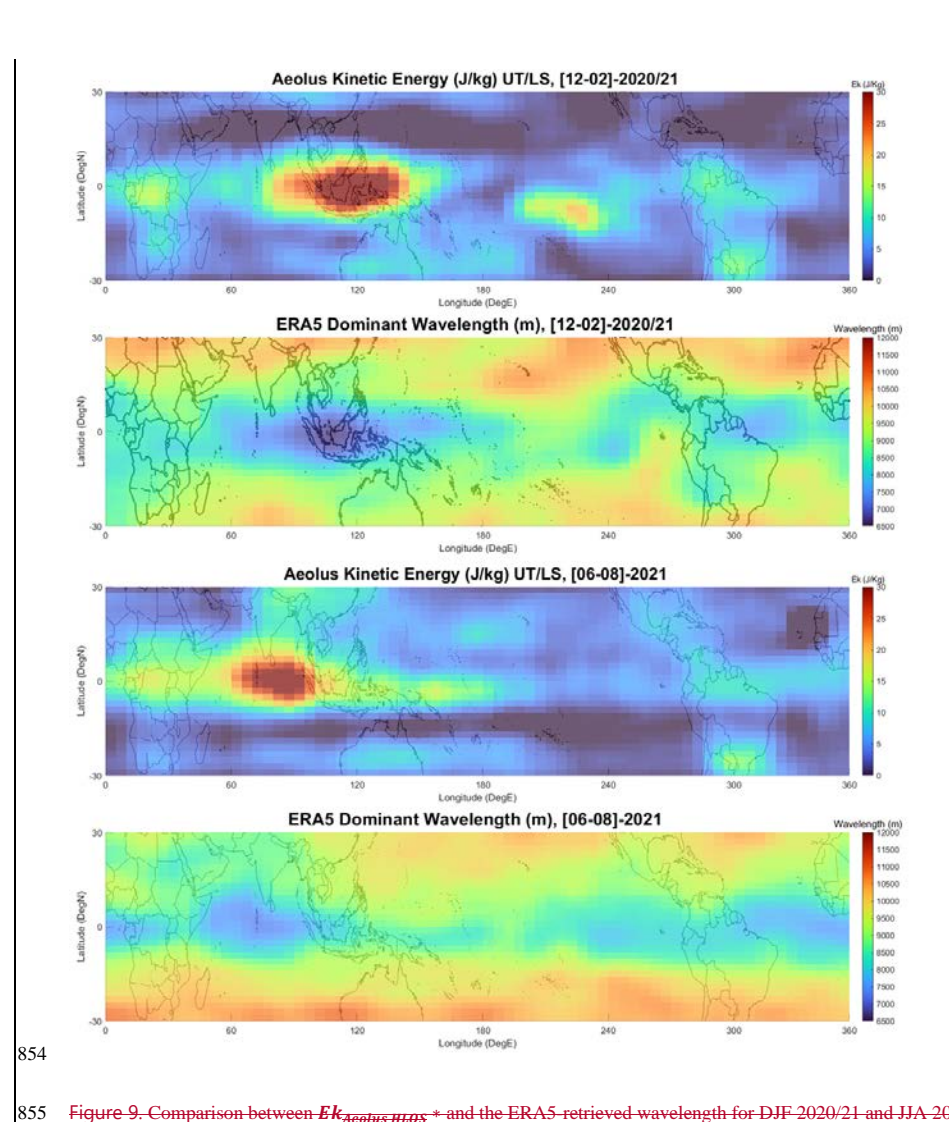


Figure 9. Comparison between *Ek_{Acotus HLOS}* * and the ERA5 retrieved wavelength for DJF 2020/21 and JJA 2021.

856

Mis en forme : Justifié, Espace Avant : Automatique, Après : Automatique

Mis en forme : Normal, Gauche, Espace Avant : Automatique, Après : Automatique

Mis en forme : Espace Avant : Automatique, Après : Automatique

858 859 Figure 9 presents a comparison between Ekasatus HLOS * and the corresponding wavelengths retrieved from ERA5 during DJF 860 2020/21 and JJA 2021. In regions around convective spots, where Acolus is shown to possess the highest EK, ERA5 displays 861 the lowest wavelength characteristics. This is expected, as waves with higher EK values are correlated with lower wavelengths. 862 Furthermore, gravity waves generated by convective processes often exhibit shorter horizontal wavelengths (Kalisch et al., 863 2016), particularly those under 100 km, which poses a challenge for retrieval by instruments like Acolus. 864 865 Waves with high EK are typically generated in regions with strong convective updrafts and downdrafts, where the rapid vertical 866 movement of air masses creates intense small-scale disturbances. These localized and transient disturbances, arising from 867 geostrophic imbalance, generate GWs that carry energy away from the convective region, where strong forcing efficiently transfers energy into the EK spectrum at shorter wavelengths (Waite and Snyder, 2009). The correlation between high EK and 868 869 shorter wavelengths is particularly pronounced in convective systems, as confirmed in both observational and numerical 870 estimations (Kalisch et al., 2016), especially in tropical regions and cyclones (Chane Ming et al., 2014). 871 872 Sensitivity studies on ERA5 data, with and without Welch windowing and frequency filtering, showed that removing the 873 Welch windowing augmented overall values and produced less confined hotspots, suggesting spectral leakage. Without high-874 pass frequency filtering (or low pass wavelength filtering), the dominant wavelengths detected are significantly longer than 875 what Aeolus can resolve, reinforcing the necessity of filtering. 876 5. Discussion 877 Overall, the results presented in this study allow us to discuss and address two main questions. The first consistent observation 878 made, was that ERA5 underestimates Ek distribution in such regions compared to the Aeolus-derived energy, particularly over 879 the Indian Ocean, where conventional radiosonde wind measurements are very sparse. That difference raised questions on the 880 potential reason for such discrepancies: Is this result an overestimation of Aeolus, due to its known increased noise and 881 inconsistent performance during its life-cycle, or an underestimation for ERA5, due to the lack of direct wind observations

857

882

assimilated?

883 The analysis of ALADIN wind profiling and ECMWF ERA5 reanalysis data, provided in Fig. 24 and Fig. 25, revealed enhanced 884 GW activity over the Indian Ocean during Boreal Summer, as well as over the western Pacific and maritime continent in Boreal 885 Winter. The enhanced GW activity migrating from eastern Africa to the Pacific maritime continent between June and 886 December is linked to convection, as suggested by the correlation between enhanced GW Ek and the regional minima in OLR. 887 The slow eastward propagation of these energy maxima suggests that the underlying wave sources are not random, but are 888 organized by planetary-scale atmospheric patterns, Indeed, the relation between OLR and the Madden-Julian Oscillation 889 (MJO) has been used before; It is a reliable index for analysis (Kiladis et al., 2014), and recent work has provided direct 890 observational evidence that the MJO modulates GW activity and momentum transport from the tropics to higher 891 latitudes (Zhou et al., 2024). The structures observed by Aeolus are therefore highly consistent with the kinetic energy signature 892 of gravity waves generated by the powerful thermal and mechanical forcing mechanisms (Beres et al., 2005; Corcos et al., 893 2025) occurring within the large, organized convective superclusters of the MJO. The enhanced GW activity migrating from 894 eastern Africa to the Pacific maritime continent between June and December is linked to convection, as suggested by the 895 correlation between enhanced GW Ek and the regional minima in OLR. The relation between OLR and the MJO has been 896 used before; It is a reliable index for analysis (Kiladis et al., 2014), hinting towards the possibility for the active phase of the 897 MJO to generate the observed hotspots through its convective activity. This suggests that Aeolus is effectively capturing 898 convection-induced GWs that may be underrepresented in ERA5. One of the persistent features observed throughout the study 899 was the high-energy gravity wave hotspot over the African continent, which remained consistent across seasons and years. 900 This suggests a continuous mechanism of continental convection driving gravity wave activity in this region.

902 could be an artifact of misinterpreting non-wave tropospheric outflow rather than stratospheric gravity waves. Our sensitivity 903 analysis (see Fig. B1 and B2 in Appendix B) directly refutes this concern. By shifting the analysis layer upward to begin 1 km 904 and 2 km above the tropopause, we confirm that the geographical patterns of the energy hotspots are remarkably stable (spatial 905 correlation r > 0.83), and that the vast majority of the peak energy (~88-91%) persists well into the stratosphere. If the signal 906 were dominated by shallow tropospheric outflow, the energy peaks would have collapsed when the analysis layer was moved 907 above the tropopause. The fact that a strong, structured signal remains provides compelling evidence that we are observing 908 vertically propagating gravity waves that have penetrated the lower stratosphere. This validates our central conclusion: Aeolus 909 is capturing a significant field of convectively-generated stratospheric gravity wave kinetic energy that is largely absent in the

Another consideration in this study is whether the large Ek values observed by Aeolus, particularly over convective hotspots,

910 ERA5 reanalysis.

901

911

912

An additional tool at our disposal to solve the case is the global distribution of Ep, through the use of independent GNSS-RO instruments. Our analysis confirms that the assimilation of GNSS-RO data in ERA5 is highly effective, with minimal discrepancies observed between the reanalysis Ep and direct GNSS-RO observations (Fig.7c). This key finding allows us to

Mis en forme: Espace Avant: 0 pt, Après: 13,5 pt, Motif: Transparente (Blanc)

arbitrate between two potential causes for the Ek discrepancy; a lack of direct wind data assimilation versus inherent biases in the model's physics (e.g., its GWD parameterization). 916 Several lines of evidence from our study point towards the lack of wind assimilation as the dominant cause. Firstly, the fact 917 that ERA5 accurately reproduces Ep fields demonstrates that the underlying model can represent the thermodynamic 918 signatures of wave activity when properly constrained. Conversely, the largest discrepancies are found in kinetic energy, a 919 purely wind-based quantity, and are concentrated over data-sparse regions like the Indian Ocean, precisely where Aeolus 920 provides direct wind profile measurements not available from other observing systems (Banyard et al., 2021). 921 Secondly, while ERA5's non-orographic GWD scheme has known limitations and is not directly forced by diagnosed 922 convection (Orr et al., 2010), it is unlikely to be the sole reason for the missing Ek. Such a parameterization bias would be 923 expected to manifest as a systematic error across different variables or regions, or as a persistent model drift requiring large, 924 ongoing corrections by the assimilation system (Dee, 2005). However, our findings show a targeted deficiency: the model 925 performs well on assimilated temperature (Ep) but poorly on unassimilated wind (Ek) in the very same locations. This sharp 926 contrast strongly suggests the problem is not a wholesale failure of the model's physics to generate wave energy, but rather its 927 inability to correctly partition that energy into kinetic and potential components without direct wind constraints. 928 In data-sparse areas, ERA5 must rely on its internal background error covariances to infer wind adjustments from the 929 assimilated mass field (Hersbach et al., 2020). These statistical relationships are primarily designed to represent large-scale, 930 quasi-balanced (rotational) flow and are known to be less effective at specifying the smaller-scale, divergent component of the 931 wind field to which convectively generated gravity waves belong, especially in the tropics (Žagar et al., 2004). Consequently, 932 while the assimilation of GNSS-RO constrains the thermodynamic (Ep) aspect of the wave, the system lacks the necessary 933 information and dynamic constraints to generate the corresponding divergent wind perturbations, leading to the 934 observed Ek deficit. This process evidently fails to capture the full spectrum of high-Ek wave modes generated by convection. 935 An additional tool at our disposal to solve the case is the global distribution of Ep, through the use of independent GNSS-RO instruments. Our initial quarterly comparisons with GNSS RO data, shown in Fig.6, revealed that Aeolus performs well, 936 937 capturing similar values in the same regions all things considered, as these two results have a lot of inherent differences 938 (different line of sight and signal projection, different physical quantities and their varying ratio, different signal treatment and 939 correction). We also found that the assimilation is nearly perfect for Ep, with minimal discrepancies between ERA5 and GNSS-940 RO (see Fig.7c). The result does not come as surprising, as ERA5 assimilates GNSS-RO in great proportions but does not have 941 any Aeolus data collected. This last hint proves that ERA5 shows no general difficulty at reproducing areas of convection 942 when it has been exposed to enough data assimilation (Ep-driven convective areas in that case). 943 Overall, the findings presented here are in full agreement with the elements outlined in the introduction, suggesting that ERA5

is underestimating the Ek component. Indeed, ERA5 has several known shortcomings, such as its underrepresentation of

eastward-propagating inertio-gravity waves (Bramberger et al., 2022), its site-dependent errors in tropical regions (Campos et

944 945 946 al., 2022), and the broader limitations of data assimilation systems in capturing circulation dynamics, particularly in areas with 947 sparse wind observations (Podglajen et al., 2014; Žagar et al., 2004). These challenges are further emphasized by the QBO-948 MJO modulation of the wave activity in the UTLS, possibly at play in the amplitude variability of the seasonal signals seen in Fig.5a, where some years show an increased activity compared to others. An observational study revealed how gravity waves 949 generated during MJO phases interact with QBO-modulated wind patterns, influencing their dissipation and energy dispersion 950 951 (Kalisch et al., 2018). The OBO easterly phase (EOBO) has been shown to enhance MJO activity by strengthening convective 952 signals and reinforcing the propagation of Rossby and Kelvin waves in the UTLS, while the westerly phase (WQBO) 953 suppresses these dynamics (Song and Wu, 2020; Martin et al., 2021). However, the limitations of ERA5 in capturing OBO-954 MJO interactions are evident, as reanalysis datasets often fail to fully reproduce the observed temperature and wind anomalies 955 associated with these processes, particularly in tropical regions (Lim and Son, 2022).

Another discussion enabled by Aeolus observations concerns the longstanding assumption of a constant Ek/Ep ratio in GW studies. Specifically, the question arises: Is the conventional view of a constant ratio for inferring Ep from Ek (and vice versa) still tenable? Or do the new data suggest that this ratio is no longer universally valid in real-world, often non-linear, atmospheric

959 conditions?

- At first glance, using a fixed ratio appears straightforward for converting well-documented Ep (from temperature-based instruments such as GNSS-RO) to Ek. Traditionally, linear GW theory proposes a near-constant ratio of Ek to Ep, often quoted between 5/3 and 2.0 (VanZandt, 1985; Hei et al., 2008). In idealized models of linear wave behavior, the kinetic and potential energies are expected to be comparable, leading to a ratio close to unity. This has been confirmed previously, in a study such as Nastrom et al. (2000), which found that in stable, linear wave conditions, the energy ratios adhered closely to these theoretical predictions.
- However, a growing body of evidence challenges this simplification: Empirical work increasingly reveals significant 966 967 variability in this ratio, indicating non-linear effects in real-world atmospheric conditions (Baumgarten et al., 2015; Guharay 968 et al., 2010; Tsuda et al., 2004). When the observed energy ratios deviate significantly from this expected range, non-linear 969 processes may be at play. For instance, in situations where wave amplitudes are particularly large, wave-wave interactions, 970 such as those resulting from wave breaking or saturation, could lead to the observed discrepancies. This has been demonstrated 971 in earlier work by Mack and Jay. (1967), who found that under certain conditions, potential energy deviated markedly from kinetic energy, suggesting non-linear effects. Similar findings have been reported by Fritts et al. (2009), who showed that 973 interactions between gravity waves and fine atmospheric structures can result in turbulence, thereby affecting the balance 974 between kinetic and potential energy.
- With everything in place to link these elements, the observed comparison in Fig. 48 of the Ek/Ep ratios from ERA5, Aeolus, and GNSS-RO confirms that the characteristics of gravity waves vary significantly across time and space. The observed ratios,

1.7 (+/- 0.38) 1.43 (+/- 0.76) for ERA5, 1.4 (+/- 0.54) 1.63 (+/- 0.7) for Aeolus/GNSS-RO, indicate that the waves encompass both linear and non-linear processes. The frequent observation of ratios exceeding unity, aligning with trends identified in previous studies, suggests that a substantial portion of the waves' energy is contained in kinetic form, often indicative of nonlinear behavior. Because the assumption of a constant ratio is increasingly challenged by empirical observations, it accentuates the need to shift the paradigm from relying solely on temperature perturbations to directly deriving Ek. As such, directly measuring kinetic energy is, and has always been, a major missing link for a comprehensive understanding of GW dynamics.

977

978

979

980

981

982

992

993 994

995

997

998

999

1000

001

003

004

005

007

008

983 Beyond these considerations of gravity wave dynamics and energy ratios, we should also acknowledge the limitations of the 984 Aeolus satellite. These include both its technical shortcomings and the constraints imposed by its HLOS projection, which directly impact the representativeness of its measurements. A 1.6 ratio was determined for Ek/Ek_{HLOS} using ERA5, as seen in 985 Fig.2. It reflects the efficiency with which HLOS winds from Aeolus can approximate the full kinetic energy field. The ratio 986 987 indicates that HLOS winds account for approximately 62.5% of the total Ek, while the remaining 37.5% is undetectable due 988 to the projection limitations of HLOS measurements. The discrepancy suggests that the HLOS winds alone cannot fully capture 989 the energy contributions from multi-dimensional wave dynamics. However, this ratio can help estimate the full Ek indirectly 990 with reasonable accuracy. While this approach introduces some assumptions, it can be further refined by cross-validating 991 against comprehensive datasets from reanalyseis models-like ERA5.

The spatial and temporal consistency observed between Aeolus and ERA5 datasets highlight the potential of Aeolus wind profiling for assimilation to improve our understanding of atmospheric dynamics in the tropical UTLS. However, there are limitations and uncertainties to consider; these include dark currents in its charge-coupled devices, known as "hot pixels", which can induce speed measurement errors of several meters per second (Weiler et al., 2021). Additionally, oscillating 996 perturbations within the instrument can cause signal deformations, potentially misinterpreted as GW-induced signals (Ratynski et al., 2023). Even though corrections have been implemented, Fig.3 showed that the instrument's overall signal random error still fluctuates due to its degradation. While newer baselines such as the latest 2B16 used in this study, improve on the appearance rate of hot pixels, challenges remain in consistently identifying and correcting other issues such as oscillating perturbations, increased solar activity, or cloud contamination that can sporadically deform signals.

002 Understanding the vertical wavelength of convective GWs is an essential element for characterizing their dynamics. However, Aeolus is inherently limited in retrieving accurate vertical wavelengths due to its design. The placement of range bins was fixed at the time of observation, introducing inconsistencies in vertical resolution that affect the precise identification of wave peaks and troughs. Additionally, the N/P parameter, which controls the number of accumulated measurements (N) and pulses 006 (P) per cycle, introduces variability in the horizontal resolution of Aeolus data. Changes to this setting, such as the transition from N=30 to N=5, improve horizontal resolution but exacerbate the misrepresentation of vertical wave structures. Furthermore, any spectral analysis of a finite vertical profile is inherently constrained. For geophysical spectra that are typically 1009 having more variance at longer wavelengths, a simple peak-finding method would likely identify a dominant wavelength that 010 is an artifact of the analysis window or filtering choices. Given these limitations, we limit our analysis to the vertically-011 integrated energy within a defined passband (vertical wavelengths < 9 km), which is a more robust quantity. 012 013 Nevertheless, we can speculate that the high Ek values observed by Aeolus in convective regions are associated with shorter-014 wavelength waves. This interpretation is consistent with established physical mechanisms which state that waves with high 015 EK are typically generated in regions with strong convective updrafts and downdrafts, where the rapid vertical movement of 016 air masses creates intense small-scale disturbances. These localized and transient disturbances, arising from geostrophic 017 imbalance, generate GWs that carry energy away from the convective region, where strong forcing efficiently transfers energy 018 into the EK spectrum at shorter wavelengths (Waite and Snyder, 2009). The correlation between high EK and shorter 019 wavelengths is particularly pronounced in convective systems, as confirmed in both observational and numerical estimations 020 (Kalisch et al., 2016), especially in tropical regions and cyclones (Chane Ming et al., 2014). A definitive observational 021 confirmation of this from the satellite itself, however, remains a challenge due to the aforementioned limitations. 022 Looking forward, a critical application for such observations is the constraint of gravity wave momentum fluxes, which are 023 essential for global circulation models. However, deriving momentum flux estimates directly from single-024 component wind measurements like those from Aeolus presents significant theoretical and observational challenges. The 025 vertical flux of horizontal momentum (e.g., \(\lambda'\text{w'}\rangle\) fundamentally requires simultaneous knowledge of both horizontal (u') and 026 vertical (w') wind perturbations. Aeolus provides only a projection of the horizontal wind and, crucially, contains no direct 027 information on the vertical wind; in fact, w' is assumed to be negligible in the standard data processing (Krisch et al., 2022). 028 This represents the primary missing piece of information for a direct flux calculation. 029 A potential pathway to overcome this limitation involves creating synergistic datasets, for instance by combining Aeolus wind 030 data with simultaneous, collocated temperature measurements from instruments like GNSS-RO. In principle, gravity wave 031 polarization relations could then be used to infer the missing wind components. However, this approach is not a simple remedy 032 and relies on strong, often unverifiable, assumptions about unmeasured wave parameters, including the horizontal wavelength, 033 intrinsic frequency, and the stationarity of the wave field between measurements (Alexander et al., 2008a; Chen et al., 2022). 034 Therefore, while Aeolus does not directly measure momentum flux, its unprecedented global measurements of kinetic energy 035 provide an additional observational constraint. Such observations are a critical prerequisite for developing and testing the more 1036 complex, multi-instrument techniques that will be required to eventually constrain the global gravity wave momentum budget.

Mis en forme : Espace Avant : Automatique, Après : 13,5 pt, Interligne : Au moins 15 pt, Motif : Transparente (Blanc)

6. Conclusion

1037

In this study, we examined the capacity of the Aeolus ALADIN instrument to capture and resolve GWs in tropical UTLS.

While this task might appear challenging at first, because of the data alteration issues Aeolus faced during its lifecycle, the

study proposed a noise correction process, which used ERA5 reanalysis as a reference to estimate and correct for Aeolus's instrument-induced variance. This correction improved the retrieving of kinetic energy, and our comparison with collocated radiosonde data further validated that approach. A key focus of our analysis was the ratio between kinetic and potential energies (Ek/Ep), providing insights into the linear or non-linear nature of these waves. The wavelength retrieval aspect also emerged as a limitation for Aeolus, reflecting constraints in the bin settings and horizontal integration of its HLOS wind measurements.

1045 The principal findings can be summarized as follows:

- Aeolus observations capture significant kinetic energy enhancements over tropical convection hotspots, particularly
 over the Indian Ocean, where ERA5 shows substantial underrepresentation due to sparse wind observations.
- Direct wind data from Aeolus could significantly enhance tropical UTLS reanalysis products, particularly in convection-driven GW regimes, reducing biases in Ek representation.
- In many regions with strong convective forcing, Aeolus data suggest a larger kinetic energy component, pointing to
 wave breaking, saturation, and other non-linear processes that depart from purely linear wave dynamics.
- While linear GW theory often prescribes an Ek/Ep ratio between ~1.6 and ~2.0, our results show that this ratio can
 vary significantly, depending on location and season. This highlights the need for direct kinetic-energy measurements
 rather than relying solely on temperature-derived potential energy as a proxy.
- Aeolus also helps fill this gap. However, given its HLOS projection, Aeolus underestimates the total Ek if meridional
 components are significant, reinforcing that multi-instrument approaches are mandatory for accurately characterizing
 GW fields.

Thus, this study has demonstrated the value of Aeolus Rayleigh wind profiling for observing GWs in the tropical UTLS, despite the high and time-variable random error associated with its measurements. Our findings confirm that the annual and zonal variation of GW activity in the tropical tropopause layer and lower stratosphere is modulated by deep convection, as demonstrated by Dzambo et al. (2019) and Evan et al. (2020). Furthermore, Aeolus data expose a significant need for improving the reanalysis regarding the convective GW Ek. The lack of GW-derived Ek in ERA5 is most pronounced in the Indian Ocean region, where conventional radiosonde wind measurements are relatively sparse. It is highly likely that the missing Ek in ERA5 is due to the misrepresentation of convective processes. The results also indicate that standard assumptions about the Ek/Ep ratio do not always hold, particularly under convective or otherwise non-linear conditions. Aeolus' range-bin design and horizontal integration restrict its ability to determine wavelengths with accuracy, which poses a significant

- 1071 challenge for fully capturing the characteristics of GW. This limitation highlights the need for complementary datasets, which
- 1072 could be addressed in newer iterations of the instrument. While this study delivers some insights into UTLS GW activity and
- 1073 the benefits of global wind observation, future research should continue investigating the factors contributing to the
- discrepancies observed between Aeolus and ERA5 data. The kinetic energy constraints provided here represent a novel step,
- and future missions like Aeolus-2 will be essential for developing the synergistic techniques required to ultimately quantify
- 076 the global momentum transport by these waves. Future missions like Acolus-2 are expected to build on these findings, offering
- 1077 improved coverage and advancing our understanding of atmospheric dynamics.
- 1079 Data Availability: Aeolus data are publicly available through the Aeolus online dissemination system (https://aeolus-
- 1080 ds.eo.esa.int/oads/access/). The dataset used for the realization of this study can be found at
- 1081 https://doi.org/10.5281/zenodo.8113261
- 1083 Author Contributions: Conceptualization, M.R, S.K, A.H, and M.J.A; methodology, M.R, S.K, A.H, and M.J.A.; software,
- 1084 M.R. and A.M. .; validation, M.R, S.K, A.H, and M.J.A;—original draft preparation, M.R. and S.K. .; writing—review and
- editing, M.R, S.K, A.H, M.J.A, A.M, P.K and A.M; funding acquisition, S.K, P.K. and A.M; All authors have read and agreed
- 1086 to the published version of the manuscript.
- 1088 Competing interests: The contact author has declared that none of the authors has any competing interests.
- 1090 Acknowledgments: The work by Mathieu Ratynski was carried out under a PhD fellowship co-funded by CNES and ACRI-
- 1091 ST. Additional funding has been provided via the CNES APR Aeolus project. MJA was funded by NSF grants #2110002 and
- 1092 #1642644.

1078

1082

1087

1089

1093 References

- 1094 Alexander, M. J. and Ortland, D. A.: Equatorial waves in High Resolution Dynamics Limb Sounder (HIRDLS) data, J.
- 1095 Geophys. Res. Atmospheres, 115, https://doi.org/10.1029/2010JD014782, 2010.
- 1096 Alexander, M. J., Gille, J., Cavanaugh, C., Coffey, M., Craig, C., Eden, T., Francis, G., Halvorson, C., Hannigan, J., Khosravi,
- 1097 R., Kinnison, D., Lee, H., Massie, S., Nardi, B., Barnett, J., Hepplewhite, C., Lambert, A., and Dean, V.: Global estimates of
- 1098 gravity wave momentum flux from High Resolution Dynamics Limb Sounder observations, J. Geophys. Res. Atmospheres,
- 1099 113, https://doi.org/10.1029/2007JD008807, 2008a.
- 1100 Alexander, M. J., Liu, C. C., Bacmeister, J., Bramberger, M., Hertzog, A., and Richter, J. H.: Observational Validation of
- 1101 Parameterized Gravity Waves From Tropical Convection in the Whole Atmosphere Community Climate Model, J. Geophys.
- 1102 Res. Atmospheres, 126, e2020JD033954, https://doi.org/10.1029/2020JD033954, 2021.

- 1103 Alexander, S., Tsuda, T., and Kawatani, Y.: COSMIC GPS Observations of Northern Hemisphere winter stratospheric gravity
- 1104 waves and comparisons with an atmospheric general circulation model, Geophys. Res. Lett. GEOPHYS RES LETT, 35,
- 1105 https://doi.org/10.1029/2008GL033174, 2008b.
- 1106 Alexander, S. P., Tsuda, T., and Kawatani, Y.: COSMIC GPS Observations of Northern Hemisphere winter stratospheric
- 1107 gravity waves and comparisons with an atmospheric general circulation model, Geophys. Res. Lett., 35,
- 1108 https://doi.org/10.1029/2008GL033174, 2008c.
- 1109 Alexander, S. P., Tsuda, T., Kawatani, Y., and Takahashi, M.: Global distribution of atmospheric waves in the equatorial upper
- 1110 troposphere and lower stratosphere: COSMIC observations of wave mean flow interactions, J. Geophys. Res. Atmospheres,
- 1111 113, https://doi.org/10.1029/2008JD010039, 2008d.
- 1112 Baker, W. E., Atlas, R., Cardinali, C., Clement, A., Emmitt, G. D., Gentry, B. M., Hardesty, R. M., Källén, E., Kavaya, M. J.,
- 1113 Langland, R., Ma, Z., Masutani, M., McCarty, W., Pierce, R. B., Pu, Z., Riishojgaard, L. P., Ryan, J., Tucker, S., Weissmann,
- 1114 M., and Yoe, J. G.: Lidar-Measured Wind Profiles: The Missing Link in the Global Observing System, Bull. Am. Meteorol.
- 1115 Soc., 95, 543–564, https://doi.org/10.1175/BAMS-D-12-00164.1, 2014.
- 1116 Banyard, T. P., Wright, C. J., Hindley, N. P., Halloran, G., Krisch, I., Kaifler, B., and Hoffmann, L.: Atmospheric Gravity
- 1117 Waves in Aeolus Wind Lidar Observations, Geophys. Res. Lett., 48, e2021GL092756,
- 1118 https://doi.org/10.1029/2021GL092756, 2021.
- 1119 Baumgarten, G., Fiedler, J., Hildebrand, J., and Lübken, F.-J.: Inertia gravity wave in the stratosphere and mesosphere observed
- 1120 by Doppler wind and temperature lidar, Geophys. Res. Lett., 42, 10,929-10,936, https://doi.org/10.1002/2015GL066991, 2015.
- 1121 Bramberger, M., Alexander, M. J., Davis, S., Podglajen, A., Hertzog, A., Kalnajs, L., Deshler, T., Goetz, J. D., and Khaykin,
- 1122 S.: First Super-Pressure Balloon-Borne Fine-Vertical-Scale Profiles in the Upper TTL: Impacts of Atmospheric Waves on
- 1123 Cirrus Clouds and the OBO, Geophys. Res. Lett., 49, e2021GL097596, https://doi.org/10.1029/2021GL097596, 2022.
- 1124 Campos, R. M., Gramcianinov, C. B., de Camargo, R., and da Silva Dias, P. L.: Assessment and Calibration of ERA5 Severe
- 1125 Winds in the Atlantic Ocean Using Satellite Data, Remote Sens., 14, 4918, https://doi.org/10.3390/rs14194918, 2022.
- 1126 Cao, B., Haase, J. S., Murphy, M. J., Alexander, M. J., Bramberger, M., and Hertzog, A.: Equatorial waves resolved by balloon-
- 127 borne Global Navigation Satellite System radio occultation in the Strateole-2 campaign, Atmospheric Chem. Phys., 22, 15379-
- 1128 15402, https://doi.org/10.5194/acp-22-15379-2022, 2022.
- 1129 Chane Ming, F., Ibrahim, C., Barthe, C., Jolivet, S., Keckhut, P., Liou, Y.-A., and Kuleshov, Y.: Observation and a numerical
- 1130 study of gravity waves during tropical cyclone Ivan (2008), Atmospheric Chem. Phys., 14, 641-658,
- 1131 https://doi.org/10.5194/acp-14-641-2014, 2014.
- 1132 Chen, O., Ntokas, K., Linder, B., Krasauskas, L., Ern, M., Preusse, P., Ungermann, J., Becker, E., Kaufmann, M., and Riese,
- 1133 M.: Satellite observations of gravity wave momentum flux in the mesosphere and lower thermosphere (MLT): feasibility and
- 1134 requirements, Atmospheric Meas. Tech., 15, 7071–7103, https://doi.org/10.5194/amt-15-7071-2022, 2022.
- 135 Danzer, J., Pieler, M., and Kirchengast, G.: Closing the gap in the tropics: the added value of radio-occultation data for wind
- 1136 field monitoring across the equator, Atmospheric Meas. Tech. Discuss., 1–19, https://doi.org/10.5194/amt-2023-137, 2023.
- 137 Dee, D. P.: Bias and data assimilation, Q. J. R. Meteorol. Soc., 131, 3323–3343, https://doi.org/10.1256/qj.05.137, 2005.

Mis en forme : Français (France)

- 1138 Dhaka, S. K., Yamamoto, M. K., Shibagaki, Y., Hashiguchi, H., Fukao, S., and Chun, H.-Y.: Equatorial Atmosphere Radar
- 1139 observations of short vertical wavelength gravity waves in the upper troposphere and lower stratosphere region induced by
- 1140 localized convection, Geophys. Res. Lett., 33, https://doi.org/10.1029/2006GL027026, 2006.
- 1141 Dzambo, A. M., Hitchman, M. H., and Chang, K.-W.: The Influence of Gravity Waves on Ice Saturation in the Tropical
- 1142 Tropopause Layer over Darwin, Australia, Atmosphere, 10, 778, https://doi.org/10.3390/atmos10120778, 2019.
- 1143 Ern, M., Preusse, P., Alexander, M. J., and Warner, C. D.: Absolute values of gravity wave momentum flux derived from
- 1144 satellite data, J. Geophys. Res. Atmospheres, 109, https://doi.org/10.1029/2004JD004752, 2004.
- 1145 Ern, M., Trinh, Q. T., Preusse, P., Gille, J. C., Mlynczak, M. G., Russell III, J. M., and Riese, M.: GRACILE: a comprehensive
- 1146 climatology of atmospheric gravity wave parameters based on satellite limb soundings, Earth Syst. Sci. Data, 10, 857–892,
 - 47 https://doi.org/10.5194/essd-10-857-2018, 2018.
- 1148 Evan, S., Brioude, J., Rosenlof, K., Davis, S. M., Vömel, H., Héron, D., Posny, F., Metzger, J.-M., Duflot, V., Payen, G.,
- 1149 Vérèmes, H., Keckhut, P., and Cammas, J.-P.: Effect of deep convection on the tropical tropopause layer composition over the
- 1150 southwest Indian Ocean during austral summer, Atmospheric Chem. Phys., 20, 10565–10586, https://doi.org/10.5194/acp-20-
- 1151 10565-2020, 2020.
- 1152 Fritts, D. C. and Alexander, M. J.: Gravity wave dynamics and effects in the middle atmosphere, Rev. Geophys., 41,
- 1153 https://doi.org/10.1029/2001RG000106, 2003.
- 1154 Fritts, D. C., Wang, L., and Werne, J.: Gravity wave-fine structure interactions: A reservoir of small-scale and large-scale
- 1155 turbulence energy, Geophys. Res. Lett., 36. https://doi.org/10.1029/2009GL039501, 2009.
- 1156 Fröhlich, K., Schmidt, T., Ern, M., Preusse, P., de la Torre, A., Wickert, J., and Jacobi, Ch.: The global distribution of gravity
- 1157 wave energy in the lower stratosphere derived from GPS data and gravity wave modelling: Attempt and challenges, J.
- 1158 Atmospheric Sol.-Terr. Phys., 69, 2238–2248, https://doi.org/10.1016/j.jastp.2007.07.005, 2007.
- 1159 Geldenhuys, M., Kaifler, B., Preusse, P., Ungermann, J., Alexander, P., Krasauskas, L., Rhode, S., Woiwode, W., Ern, M.,
- 1160 Rapp, M., and Riese, M.: Observations of Gravity Wave Refraction and Its Causes and Consequences, J. Geophys. Res.
- 1161 Atmospheres, 128, e2022JD036830, https://doi.org/10.1029/2022JD036830, 2023.
- 1162 Gubenko, V. N., Pavelyev, A. G., Salimzyanov, R. R., and Andreev, V. E.: A method for determination of internal gravity
 - wave parameters from a vertical temperature or density profile measurement in the Earth's atmosphere, Cosm. Res., 50, 21–
- 1164 31, https://doi.org/10.1134/S0010952512010029, 2012.
- 1165 Guharay, A., Venkat Ratnam, M., Nath, D., and Dumka, U. C.: Investigation of saturated gravity waves in the tropical lower
- atmosphere using radiosonde observations, Radio Sci., 45, https://doi.org/10.1029/2010RS004372, 2010.
- 1167 Hei, H., Tsuda, T., and Hirooka, T.: Characteristics of atmospheric gravity wave activity in the polar regions revealed by GPS
- 1168 radio occultation data with CHAMP, J. Geophys. Res. Atmospheres, 113, https://doi.org/10.1029/2007JD008938, 2008.
- 1169 Hersbach, H., Bell, B., Berrisford, P., Hirahara, S., Horányi, A., Muñoz-Sabater, J., Nicolas, J., Peubey, C., Radu, R., Schepers,
- 170 D., Simmons, A., Soci, C., Abdalla, S., Abellan, X., Balsamo, G., Bechtold, P., Biavati, G., Bidlot, J., Bonavita, M., De Chiara,
- 1171 G., Dahlgren, P., Dee, D., Diamantakis, M., Dragani, R., Flemming, J., Forbes, R., Fuentes, M., Geer, A., Haimberger, L.,
- 1172 Healy, S., Hogan, R. J., Hólm, E., Janisková, M., Keeley, S., Laloyaux, P., Lopez, P., Lupu, C., Radnoti, G., de Rosnay, P.,
- 1173 Rozum, I., Vamborg, F., Villaume, S., and Thépaut, J.-N.: The ERA5 global reanalysis, O. J. R. Meteorol. Soc., 146, 1999-
- 1174 2049, https://doi.org/10.1002/qj.3803, 2020.

- $1175 \quad Holloway, C.\ E.\ and\ Neelin, J.\ D.:\ The\ Convective\ Cold\ Top\ and\ Quasi\ Equilibrium,\ https://doi.org/10.1175/JAS3907.1,\ 2007.$
- 1176 John, S. R. and Kumar, K. K.: A discussion on the methods of extracting gravity wave perturbations from space-based
- measurements, Geophys. Res. Lett., 40, 2406–2410, https://doi.org/10.1002/grl.50451, 2013.
- 1178 Kalisch, S., Chun, H.-Y., Ern, M., Preusse, P., Trinh, Q. T., Eckermann, S. D., and Riese, M.: Comparison of simulated and
- 1179 observed convective gravity waves, J. Geophys. Res. Atmospheres, 121, 13,474-13,492,
- 1180 https://doi.org/10.1002/2016JD025235, 2016.
- 1181 Kalisch, S., Kang, M.-J., and Chun, H.-Y.: Impact of Convective Gravity Waves on the Tropical Middle Atmosphere During
- the Madden-Julian Oscillation, J. Geophys. Res. Atmospheres, 123, 8975–8992, https://doi.org/10.1029/2017JD028221, 2018.
- 1183 Khaykin, S. M., Hauchecorne, A., Mzé, N., and Keckhut, P.: Seasonal variation of gravity wave activity at midlatitudes from
- 1184 7 years of COSMIC GPS and Rayleigh lidar temperature observations, Geophys. Res. Lett., 42, 1251-1258,
- 1185 https://doi.org/10.1002/2014GL062891, 2015.
- 1186 Kiladis, G., Dias, J., Straub, K., Wheeler, M., Tulich, S., Kikuchi, K., Weickmann, K., and Ventrice, M.: A Comparison of
- 187 OLR and Circulation-Based Indices for Tracking the MJO, Mon. Weather Rev., 142, 1697-1715,
- 1188 https://doi.org/10.1175/MWR-D-13-00301.1, 2014.
- 1189 Krisch, I., Hindley, N. P., Reitebuch, O., and Wright, C. J.: On the derivation of zonal and meridional wind components from
- 1190 Aeolus horizontal line-of-sight wind, Atmospheric Meas. Tech., 15, 3465–3479, https://doi.org/10.5194/amt-15-3465-2022,
- 1190 Acold
- 1192 Kumari, K., Wu, H., Long, A., Lu, X., and Oberheide, J.: Mechanism Studies of Madden-Julian Oscillation Coupling Into the
- 1193 Mesosphere/Lower Thermosphere Tides Using SABER, MERRA-2, and SD-WACCMX, J. Geophys. Res. Atmospheres, 126,
- 1194 e2021JD034595, https://doi.org/10.1029/2021JD034595, 2021.
- 1195 Ladstädter, F., Steiner, A. K., Foelsche, U., Haimberger, L., Tavolato, C., and Kirchengast, G.: An assessment of differences
- 1196 in lower stratospheric temperature records from (A)MSU, radiosondes, and GPS radio occultation, Atmospheric Meas. Tech.,
- 1197 4, 1965–1977, https://doi.org/10.5194/amt-4-1965-2011, 2011.
- 1198 Lim, Y. and Son, S.-W.: QBO Wind Influence on MJO-Induced Temperature Anomalies in the Upper Troposphere and Lower
- 1199 Stratosphere in an Idealized Model, https://doi.org/10.1175/JAS-D-21-0296.1, 2022.
- 1200 Luna, D., Alexander, P., and de la Torre, A.: Evaluation of uncertainty in gravity wave potential energy calculations through
- 1201 GPS radio occultation measurements, Adv. Space Res., 52, 879–882, https://doi.org/10.1016/j.asr.2013.05.015, 2013.
- 1202 Mack, L. R. and Jay, B. E.: The partition of energy in standing gravity waves of finite amplitude, J. Geophys. Res. 1896-1977,
- 1203 72, 573–581, https://doi.org/10.1029/JZ072i002p00573, 1967.
- 1204 MARQUARDT, C. and Healy, S.: Measurement Noise and Stratospheric Gravity Wave Characteristics Obtained from GPS
- 205 Occultation Data, J. Meteorol. Soc. Jpn. J METEOROL SOC JPN, 83, 417–428, https://doi.org/10.2151/jmsj.83.417, 2005.
- Martin, Z., Son, S.-W., Butler, A., Hendon, H., Kim, H., Sobel, A., Yoden, S., and Zhang, C.: The influence of the quasi-
- 1207 biennial oscillation on the Madden-Julian oscillation, Nat. Rev. Earth Environ., 2, 477-489, https://doi.org/10.1038/s43017-
- 1208 021-00173-9, 2021.
- 1209 Munday, C., Engelstaedter, S., Ouma, G., Ogutu, G., Olago, D., Ong'ech, D., Lees, T., Wanguba, B., Nkatha, R., Ogolla, C.,
- 1210 Gàlgalo, R. A., Dokata, A. J., Kirui, E., Hope, R., and Washington, R.: Observations of the Turkana Jet and the East African

Mis en forme : Espagnol (Amérique latine)

- 1211 Dry Tropics: The RIFTJet Field Campaign, Bull. Am. Meteorol. Soc., 103, E1828-E1842, https://doi.org/10.1175/BAMS-D-
- 1212 21-0214.1, 2022.
- 1213 Muñoz-Sabater, J., Dutra, E., Agustí-Panareda, A., Albergel, C., Arduini, G., Balsamo, G., Boussetta, S., Choulga, M.,
- 1214 Harrigan, S., Hersbach, H., Martens, B., Miralles, D. G., Piles, M., Rodríguez-Fernández, N. J., Zsoter, E., Buontempo, C.,
- 1215 and Thépaut, J.-N.: ERA5-Land: a state-of-the-art global reanalysis dataset for land applications, Earth Syst. Sci. Data, 13,
- 1216 4349–4383, https://doi.org/10.5194/essd-13-4349-2021, 2021.
- 1217 Nastrom, G. D., Hansen, A. R., Tsuda, T., Nishida, M., and Ware, R.: A comparison of gravity wave energy observed by VHF
- 1218 radar and GPS/MET over central North America, J. Geophys. Res. Atmospheres, 105, 4685-4687,
- 1219 https://doi.org/10.1029/1999JD901164, 2000.
- 1220 Orr, A., Bechtold, P., Scinocca, J., Ern, M., and Janiskova, M.: Improved Middle Atmosphere Climate and Forecasts in the
- 1221 ECMWF Model through a Nonorographic Gravity Wave Drag Parameterization, https://doi.org/10.1175/2010JCLI3490.1,
- 1222 2010.
- 1223 Pahlavan, H. A., Fu, Q., Wallace, J. M., and Kiladis, G. N.: Revisiting the Quasi-Biennial Oscillation as Seen in ERA5. Part
- 224 I: Description and Momentum Budget, https://doi.org/10.1175/JAS-D-20-0248.1, 2021.
- 1225 Plougonven, R. and Zhang, F.: Internal gravity waves from atmospheric jets and fronts, Rev. Geophys., 52, 33-76,
- 1226 https://doi.org/10.1002/2012RG000419, 2014.
- 1227 Podglajen, A., Hertzog, A., Plougonven, R., and Žagar, N.: Assessment of the accuracy of (re)analyses in the equatorial lower
- 1228 stratosphere, J. Geophys, Res. Atmospheres, 119, 11,166-11,188, https://doi.org/10.1002/2014JD021849, 2014.
- 1229 Ratynski, M., Khaykin, S., Hauchecorne, A., Wing, R., Cammas, J.-P., Hello, Y., and Keckhut, P.: Validation of Aeolus wind
- 1230 profiles using ground-based lidar and radiosonde observations at Réunion island and the Observatoire de Haute-Provence.
- 1231 Atmospheric Meas. Tech., 16, 997–1016, https://doi.org/10.5194/amt-16-997-2023, 2023.
- 1232 The NWP impact of Aeolus Level-2B Winds at ECMWF: https://www.ecmwf.int/en/elibrary/81172-nwp-impact-aeolus-level-
- 1233 2b-winds-ecmwf, last access: 16 December 2023.
- Rennie, M. P., Isaksen, L., Weiler, F., Jos de Kloe, Kanitz, T., and Reitebuch, O.: The impact of Aeolus wind retrievals on
- 1235 ECMWF global weather forecasts, Q. J. R. Meteorol. Soc., 147, 3555–3586, https://doi.org/10.1002/qj.4142, 2021.
- 1236 Šácha, P., Foelsche, U., and Pišoft, P.: Analysis of internal gravity waves with GPS RO density profiles, Atmospheric Meas.
- 1237 Tech., 7, 4123–4132, https://doi.org/10.5194/amt-7-4123-2014, 2014.
- 1238 Schmidt, T., de la Torre, A., and Wickert, J.: Global gravity wave activity in the tropopause region from CHAMP radio
- 1239 occultation data, Geophys. Res. Lett., 35, https://doi.org/10.1029/2008GL034986, 2008.
- 1240 Schmidt, T., Alexander, P., and de la Torre, A.: Stratospheric gravity wave momentum flux from radio occultations, J.
- 1241 Geophys. Res. Atmospheres, 121, 4443–4467, https://doi.org/10.1002/2015JD024135, 2016.
- 1242 Scinocca, J. F.: An Accurate Spectral Nonorographic Gravity Wave Drag Parameterization for General Circulation Models,
- 1243 2003.
- 1244 Song, L. and Wu, R.: Modulation of the Westerly and Easterly Quasi-Biennial Oscillation Phases on the Connection between
- 1245 the Madden-Julian Oscillation and the Arctic Oscillation, Atmosphere, 11, 175, https://doi.org/10.3390/atmos11020175, 2020.

- 1246 Stephan, C. C. and Mariaccia, A.: The signature of the tropospheric gravity wave background in observed mesoscale motion,
- 1247 Weather Clim. Dyn., 2, 359–372, https://doi.org/10.5194/wcd-2-359-2021, 2021.
- 1248 Tsuda, T., Nishida, M., Rocken, C., and Ware, R. H.: A Global Morphology of Gravity Wave Activity in the Stratosphere
- 1249 Revealed by the GPS Occultation Data (GPS/MET), J. Geophys. Res. Atmospheres, 105, 7257-7273,
- 1250 https://doi.org/10.1029/1999JD901005, 2000.
- 1251 Tsuda, T., Ratnam, M. V., May, P. T., Alexander, M. J., Vincent, R. A., and MacKinnon, A.: Characteristics of gravity waves
- 1252 with short vertical wavelengths observed with radiosonde and GPS occultation during DAWEX (Darwin Area Wave
- 1253 Experiment), J. Geophys. Res. Atmospheres, 109, https://doi.org/10.1029/2004JD004946, 2004.
- 1254 VanZandt, T. E.: A model for gravity wave spectra observed by Doppler sounding systems, Radio Sci., 20, 1323-1330,
- 1255 https://doi.org/10.1029/RS020i006p01323, 1985.
- 1256 Waite, M. L. and Snyder, C.: The Mesoscale Kinetic Energy Spectrum of a Baroclinic Life Cycle,
- 1257 https://doi.org/10.1175/2008JAS2829.1, 2009.
- 1258 Wang, L. and Alexander, M. J.: Global estimates of gravity wave parameters from GPS radio occultation temperature data, J.
- 1259 Geophys. Res. Atmospheres, 115, https://doi.org/10.1029/2010JD013860, 2010.
- 1260 Weiler, F., Kanitz, T., Wernham, D., Rennie, M., Huber, D., Schillinger, M., Saint-Pe, O., Bell, R., Parrinello, T., and
- 1261 Reitebuch, O.: Characterization of dark current signal measurements of the ACCDs used on board the Aeolus satellite,
- 1262 Atmospheric Meas. Tech., 14, 5153–5177, https://doi.org/10.5194/amt-14-5153-2021, 2021.
- 1263 Wright, C. J. and Hindley, N. P.: How well do stratospheric reanalyses reproduce high-resolution satellite temperature
- 1264 measurements?, Atmospheric Chem. Phys., 18, 13703–13731, https://doi.org/10.5194/acp-18-13703-2018, 2018.
- 1265 Wüst, S. and Bittner, M.: Gravity wave reflection: Case study based on rocket data, J. Atmospheric Sol.-Terr. Phys., 70, 742-
- 1266 755, https://doi.org/10.1016/j.jastp.2007.10.010, 2008.
- 1267 Yang, S.-S., Pan, C.-J., and Das, U.: Investigating the Spatio-Temporal Distribution of Gravity Wave Potential Energy over
- 1268 the Equatorial Region Using the ERA5 Reanalysis Data, Atmosphere, 12, 311, https://doi.org/10.3390/atmos12030311, 2021.
- 1269 Žagar, N., Gustafsson, N., and Källén, E.: Variational data assimilation in the tropics: The impact of a background-error
 - 70 constraint, Q. J. R. Meteorol. Soc., 130, 103–125, https://doi.org/10.1256/qj.03.13, 2004.
- 1271 Zhang, K., Randel, W. J., and Fu, R.: Relationships between outgoing longwave radiation and diabatic heating in reanalyses,
- 1272 Clim. Dyn., 49, 2911–2929, https://doi.org/10.1007/s00382-016-3501-0, 2017.
- 1273 Zhang, S. D. and Yi, F.: A statistical study of gravity waves from radiosonde observations at Wuhan (30° N, 114° E) China,
- 1274 Ann. Geophys., 23, 665–673, https://doi.org/10.5194/angeo-23-665-2005, 2005.
- 1275 Zhang, S. D., Yi, F., Huang, C. M., and Zhou, Q.: Latitudinal and seasonal variations of lower atmospheric inertial gravity
- 1276 wave energy revealed by US radiosonde data, Ann. Geophys., 28, 1065-1074, https://doi.org/10.5194/angeo-28-1065-2010,
- 1277 2010.